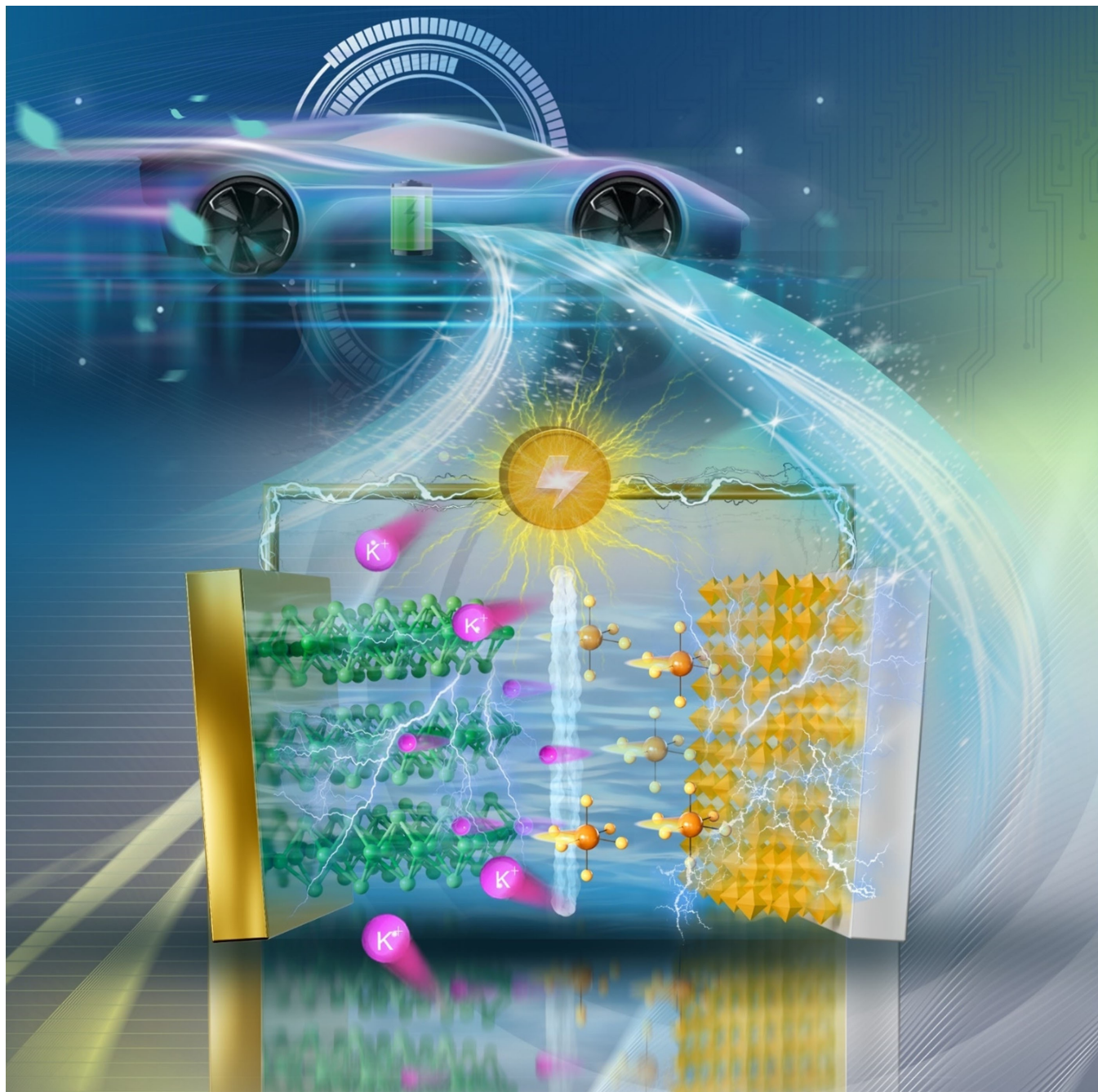


# Advanced Electrode Materials for Potassium-Ion Hybrid Capacitors

Ziyu Chen,<sup>[a]</sup> Qianqian Shen,<sup>[a]</sup> Jianzhen Xiong,<sup>[a]</sup> Jiangmin Jiang,<sup>\*[a, b]</sup> Zhicheng Ju,<sup>\*[a]</sup> and Xiaogang Zhang<sup>\*[b]</sup>



Potassium-ion hybrid capacitors (PIHCs) overcome the limitations of potassium-ion batteries (PIBs) and supercapacitors (SCs) and integrate the advantages of both, including high energy density, high power density, low cost, long cycle life, and stable electrochemical performance. However, the development of PIHCs is hindered by thermodynamic instability and kinetic hysteresis. Additionally, the dynamic mismatch between anode and cathode materials poses an urgent challenge. To this end, many research works related to material development have

been dedicated to overcoming the drawbacks. In this review, the energy storage mechanism of PIHCs is briefly introduced. Moreover, the research progress and achievements of anode and cathode materials in recent years are reviewed, including carbon-based materials, MXenes, transition metal materials, Prussian blue and its analogues. Finally, the challenges and prospects of PIHCs are proposed, together with guiding significant research directions in the future.

## 1. Introduction

With the development of society and the comprehensive progress of science and technology, the utilization ratio of electronic appliances and electric vehicles continues to increase, thus stimulating the electricity demand. The ratio of non-renewable energy in electricity generation is high. On the one hand, it will lead to the reserve crisis of fossil energy; on the other hand, a large number of harmful byproducts will be released during the consumption of fossil dyes, such as nitrogen oxides, carbon dioxide, and various heavy metal particles, which contribute to water, air and soil pollution, as well as global warming.<sup>[1]</sup> Therefore, it is urgent to vigorously develop clean, renewable energy and increase its share in electricity generation.<sup>[2]</sup> Solar and wind energy are regarded as environmentally friendly, widely distributed, and cheap renewable energy. Nevertheless, wind and photovoltaic power generation show extreme randomness and volatility, greatly influenced by weather and seasons. They seriously affect the safety and stability of power system operation and may even damage the power grid.

As an essential solution to the energy crisis, electrochemical energy storage has a rapidly expanding market size and broad development space, closely related to improving energy storage system efficiency, extending cycle life, and reducing cost.<sup>[3–6]</sup> Lithium-ion batteries (LIBs), as an essential representative of electrochemical energy storage, have the advantages of high energy density, high Coulombic efficiency, low self-discharge features, and a range of chemical potentials, accessible with diverse electrode designs.<sup>[7,8]</sup> Therefore, LIBs have been extensively applied in portable electronic devices and are crucial in powering electric vehicles and smart grids.<sup>[9–11]</sup> Nevertheless, lithium is scarce and unevenly distributed in the Earth's

crust, raising the risk of supply instability and price increases.<sup>[12]</sup> Therefore, potassium-ion batteries (PIBs) have been developed to meet the performance, cost, and other requirements for energy storage.<sup>[13–16]</sup> In the practical application of automotive power storage systems and power grid energy storage systems, there are high requirements not only for energy density but also for power density and intestinal cycle life.<sup>[17]</sup> Supercapacitors (SCs) rely on the double electric layer formed between the electrode material and electrolyte to store energy, so they can realize the rapid storage and release of energy, having the characteristics of high power and long cycle life, but their energy density is low.<sup>[18]</sup>

As a novel design, PIBs and SCs can be 'internally crossed' to construct potassium-ion hybrid capacitors (PIHCs), which can simultaneously exert the high energy density of PIBs and the high power density of SCs. In particular, PIHCs have the advantages of abundant potassium resources (Li: 0.0017%, Na: 2.6%, and K: 2.1%), low standard electrode potential, long lifespan, and low cost.<sup>[19,20]</sup> However, the development of PIHCs is restricted by thermodynamic instability and kinetic hysteresis, together with the dynamic mismatch of anode and cathode materials is an urgent problem currently. Given this, many research works on material development have been put forward to overcome the drawbacks. Meanwhile, a comprehensive review focusing on designing and modifying anode and cathode materials for PIHCs is just around the corner.

In this review, we focus on the ongoing processes of the recent development on PIHCs. The energy storage mechanism and existing issues of PIHCs are first briefly outlined. In particular, the anode and cathode materials of PIHCs, which are summarized and discussed in detail, including carbon-based materials, MXenes, transition metal materials, and Prussian blue and its analogues (Figure 1). Finally, we propose some unresolved challenges and prospects for improving the dynamic match and stability of PIHCs.

## 2. Energy Storage Mechanism of PIHCs

PIHCs combine the principles of secondary batteries and supercapacitors, and both non-Faraday and Faraday reactions occur during charging and discharging (Figure 2a and b).<sup>[17,21]</sup> During the process of charging, the potassium ions in the electrolyte are embedded in the anode. In contrast, the anions in the electrolyte are adsorbed on the surface of the cathode material to form a double layer (Figure 2c). During discharge,

[a] Dr. Z. Chen, Dr. Q. Shen, Dr. J. Xiong, Dr. J. Jiang, Prof. Z. Ju  
Jiangsu Province Engineering Laboratory of High Efficient Energy Storage  
Technology and Equipments

School of Materials Science and Physics  
China University of Mining and Technology  
Xuzhou 221116 (China)  
E-mail: jiangmin326@163.com  
juzc@cumt.edu.cn

[b] Dr. J. Jiang, Prof. X. Zhang  
Jiangsu Key Laboratory of Electrochemical Energy Storage Technology  
College of Material Science and Engineering  
Nanjing University of Aeronautics and Astronautics  
Nanjing, 210016 (China)  
E-mail: azhangxg@nuaa.edu.cn

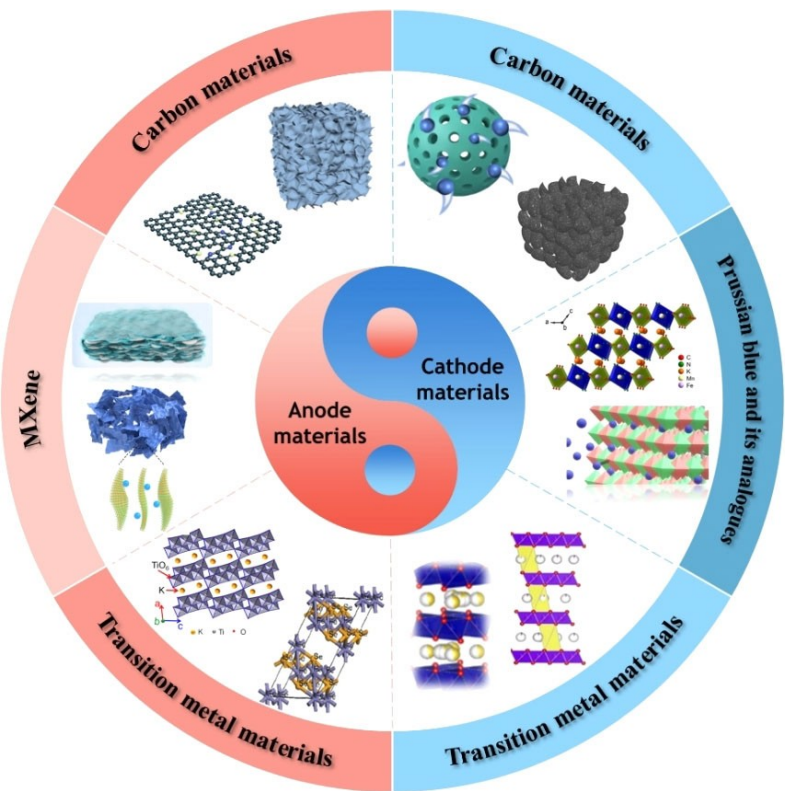


Figure 1. Classification of advanced electrode materials for PIHCs.

the potassium ions are detached from the anode material and return to the electrolyte. The double layer at the interface

between the cathode and the electrolyte dissociates, which allows the anions to be released from the surface of the



Jiangmin Jiang is a Lecturer of School of Materials Science and Physics at China University of Mining and Technology. He received his M.E. degree in 2017 and Ph.D. degree in 2021 under the supervision of Prof. Xiaogang Zhang at Nanjing University of Aeronautics and Astronautics. During 2019 to 2020, he was a co-training Ph.D under the supervision of Prof. John Wang at National University of Singapore. His research focuses on advanced materials for electrochemical energy storage devices, such as hybrid-ion capacitors, high energy batteries, and 3D current collectors.



Zhicheng Ju received his Ph.D in nanomaterials chemistry, from Shandong University in 2011 under the supervision of Prof. Yitai Qian. After postdoctoral training in School of Chemistry and Materials Science, University of Science and Technology of China from 2011 to 2013, he joined School of Materials Science and Engineering, China University of Mining and Technology as an assistant professor and was promoted to be associate professor in 2017. His research interests mainly focus on transitional metal oxides, carbon-based materials, and coal-based carbon materials, as well as on new energy materials for alkali-metal ion batteries and supercapacitors.



Xiaogang Zhang is a Professor of Chemistry in College of Material Science and Engineering at Nanjing University of Aeronautics and Astronautics, Fellow of the Royal Society of Chemistry, and the Director of Jiangsu Key Laboratory of Electrochemical Energy Storage Technology. He received his Ph.D. degree in Chemistry from Lanzhou University in 2001. His current research interests include the design and development of nanostructured composites and their applications in energy storage and conversion.

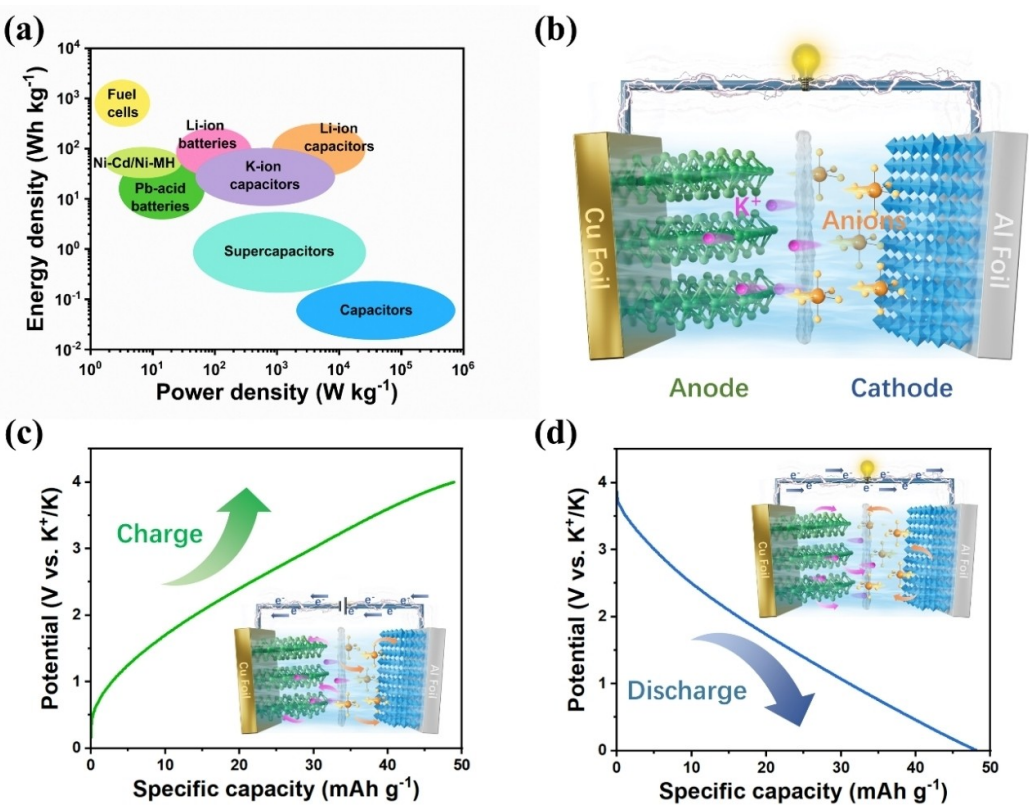


**Figure 2.** a) Energy density and power density profiles of PIHCs and other energy storage devices. b-d) Schematic illustration of the energy storage mechanism for PIHCs.

cathode material and the electrons to reach the cathode through an external circuit from the anode (Figure 2d).<sup>[22,23]</sup>

The energy densities and power densities of PIHCs can be calculated by the following equations:<sup>[24]</sup>

$$E = \int_{t1}^{t2} IVdt = \frac{1}{2}CV^2 = \frac{1}{2}C(V_{max}^2 - V_{min}^2)$$

$$C = \frac{Ixt}{m \times \Delta V}$$

$$P = \frac{E}{t}$$

Where  $I$ ,  $m$ ,  $C$ , and  $\Delta E$  are the current density, the active material mass of the cathode and anode, specific capacitance, and operating voltage window, respectively.

To achieve high-performance PIHCs, it is crucial to promote K<sup>+</sup> insertion/desorption in the anode material and to design suitable cathode materials matched to the anode.<sup>[25]</sup> The total charge stored in each electrode is determined by the specific capacitance, active mass, and potential window of each electrode. The mass ratio between anode and cathode electrodes can be calculated according to the equations:<sup>[26]</sup>

$$Q_{electrode} = C_{electrode} \times m \times \Delta E$$

$$\frac{m_+}{m_-} = \frac{C_- \times \Delta E_-}{C_+ \times \Delta E_+}$$

PIHCs can be divided into two types: (1) The battery-type electrode is used as the anode, and the capacitor-type electrode is used as the cathode. (2) The capacitor-type electrode is used as the anode, and the battery-type electrode is used as the cathode. Generally, battery-type anode materials are used to store potassium ions. The primary charge storage mode for battery-type anode materials is the intercalation reaction. In order to store more potassium ions and adapt to the volume changes caused by repeated insertion/removal of potassium ions, anode materials have ample storage space for potassium ions, smooth transportation channels, and structure.<sup>[21]</sup> The charge is stored on the surface by ion adsorption/desorption for capacitor-type cathode materials, so it should have a large specific surface area (SSA), and activated carbon (AC) is a commonly used capacitor-type cathode material.<sup>[27]</sup>

### 3. Anode Materials for PIHCs

#### 3.1. Carbon-based materials

Carbon-based material, as the most promising anode materials, which has been widely applied in PIHCs owing to its stable structure, simple preparation process, low cost, and low environmental pollution.<sup>[28-30]</sup> In this chapter, graphite, graphene, soft carbons (SCs), hard carbons (HCs), heteroatom-

doped carbons, and so on have been expounded in detail as anode materials for PIHCs.

### 3.1.1. Graphite

Graphite is a crystal form composed of stacked graphene layers with high initial Coulombic efficiency (ICE), good cycling stability, and moderate cost. The first PIHCs reported in 2017 have good electrochemical performance ( $11 \text{ Wh kg}^{-1}$  after 55 000 cycles) when using a graphite anode and an electrical double-layer capacitor (EDLC)-based activated carbon cathode.<sup>[31]</sup> Simultaneously, the comparison between the PIHCs and the symmetric EDLC further highlights the excellent electrochemical performance of graphite as an anode material, which lays a solid foundation for future scientific research.

In anode materials such as graphite, alkali ion dissolution is an obstacle to achieving high power output. A co-intercalation mechanism has been highlighted to address this issue, in which potassium ions chelate alkali metal ions using a solvent that forms a shell around the ion.<sup>[32]</sup> Incorporating ion and solvent shells into layered anodes can reduce rate-limiting solvation and facilitate ultrafast diffusion due to weak ion-host-lattice

interactions. The researchers utilized a co-intercalation graphite anode and an open framework Prussian blue cathode to achieve a moderate energy density of over  $100 \text{ Wh kg}^{-1}$  and a power density of over  $1000 \text{ W kg}^{-1}$ . However, due to the narrow interlayer spacing and large size of potassium in graphite, the barrier to potassium storage is high, slowing down the incorporation process. In addition, the formation of  $\text{KC}_8$  will cause a colossal volume expansion, which will quickly destroy the internal structure of the electrode, resulting in a rapid decrease in the specific capacitance. Besides, Meng et al. demonstrated the transformation of confined graphite into a bamboo shoot-like structure using Hummers oxidation and rapid thermal expansion with graphitic onion-like carbon (GOC).<sup>[33]</sup> The polyhedral structure and interlaced graphitic layers of GOC restrict the escape of gas, forming expanded graphitic onion-like carbon (EGOC) with a helical structure and numerous wavy wrinkles (Figure 3a). The work provides a high-performance expanded graphite electrode for developing and applying potassium-ion energy storage systems.

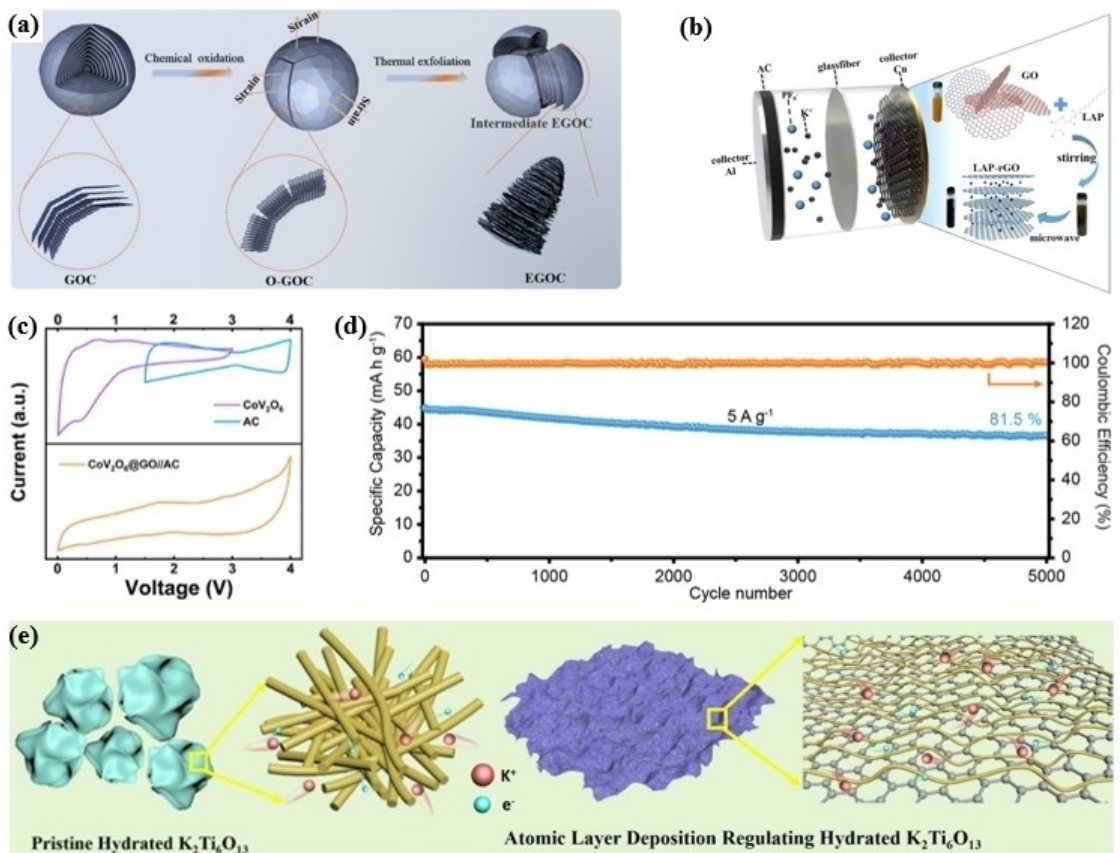


**Figure 3.** a) Schematic illustration of the preparation for EGOC. Reproduced with permission from Ref. [33]. Copyright (2022) Royal Society of Chemistry. b) Schematic diagram of PIHCs assembly and the preparation process for LAP-rGO-CDs. Reproduced with permission from Ref. [35]. Copyright (2021) Elsevier. c) CV curves of P-CVO N@GO and AC in half cells (top) and full of PIHCs (bottom). Reproduced with permission from Ref. [38]. Copyright (2019) Wiley-VCH. d) Cycling stability of PIHCs using CBC@G as an anode. Reproduced with permission from Ref. [41]. Copyright (2020) Wiley-VCH. e) Schematic illustration of pristine KTO and ALD KTO regarding electron/charge diffusion and transport. Reproduced with permission from Ref. [42]. Copyright (2021) Elsevier.

### 3.1.2. Graphene

Graphene sheets have a smaller size compared to bulk graphite, resulting in a shorter diffusion path for potassium ions between the sheets.<sup>[34]</sup> Additionally, the increase in layer spacing enhances the diffusion and magnification properties of potassium ions. Dong et al. utilized a microwave-assisted method to create LAP-rGO-CDs, which are reduced graphene oxides modified with carbon dots using L-Ascorbic acid 6-palmitate as the reducing agent (Figure 3b).<sup>[35]</sup> The introduction of carbon dots resulted in enlarged interlayer spacing and faster ion transfer rate.

Defective graphene can provide additional capacitance or faradaic charge storage.<sup>[36]</sup> On the other hand, graphene sheets with large SSA are beneficial to the dispersion of nanoparticles, prevent the recombination of graphene sheets, and reduce the van der Waals force between adjacent sheets. Li and his coworkers used pine needles and graphene oxide as precursors to create hierarchical and porous carbon/graphene networks composed of oxygen (OAC/G).<sup>[37]</sup> The graphene oxide content in the precursor has a significant effect on the morphology and structure of the derived carbon matrix composites. The in-situ oxygen doping of carbon composites widens the carbon interlayer spacing and increases the active sites on the surface of carbon composites. In addition, the energy density of the dual-carbon PIHCs with OAC/G-5 as the anode and pine needle-AC with high SSA as the cathode is as high as  $156.7 \text{ Wh kg}^{-1}$ . Furthermore, in view of the excellent potassium storage properties of current  $\text{CoV}_2\text{O}_6$  composites, porous  $\text{CoV}_2\text{O}_6$  nanospheres@GO (P-CVO-N@GO) was synthesized as the anode material. They observed an initial intercalation reaction followed by a conversion reaction during the discharge process of PIBs.<sup>[38]</sup> Benefiting from the unique nanoporous structure, the assembled PIHCs with P-CVO-N@GO anode and AC cathode achieve a high energy density of  $150.8 \text{ Wh kg}^{-1}$  and a power density of  $22500 \text{ W kg}^{-1}$  with an attractive lifetime (3000 cycles) (Figure 3c).

Heteroatom doping is a terrific way to modify graphene.<sup>[39]</sup> The synthesis of heteroatom-doped graphene usually adopts two methods: post-annealing and direct synthesis. During post-processing, graphene or graphene oxide must be extracted first and then treated in  $\text{NH}_3$  or other atmospheres. Harsh reaction conditions and toxic reactants severely limit the practical application of this process. Therefore, dual N, P heteroatom co-doped graphene (NPG) was obtained by a one-step arc discharge method using  $(\text{NH}_4)_3\text{PO}_4$  as nitrogen and phosphorus sources under the He and  $\text{H}_2$  atmosphere.<sup>[40]</sup> Large NPG nanosheets consist of 2–6 layers of graphene with P and N concentrations of 1.3 and 3.2 at.%, respectively. Full carbon-based PIHCs (NPG//AC) show capacities of  $56 \text{ mAh g}^{-1}$  at  $1 \text{ A g}^{-1}$ . A novel nitrogen-doped carbon material (CBC@G), resembling a pomegranate, was successfully synthesized using an ultrasound-assisted approach.<sup>[41]</sup> This material exhibits exceptional performance in potassium storage due to its abundant active sites and high N-6 content, which enhances its reversible specific capacity. Additionally, the connected graphene network facilitates charge transfer, resulting in improved rate capability.

The graphene network buffers CBC@G, demonstrating significant mechanical strength and exceptional cycling stability, as shown in Figure 3(d). Besides, Li et al. utilized a method of atomic layer deposition (ALD) coupled with hydrothermal potassiation to regulate hydrated  $\text{K}_2\text{Ti}_6\text{O}_{13}$  nanobelts (KTO NBs) on graphene nanosheets (Figure 3e).<sup>[42]</sup> The chemical adsorption of water increases the interlayer distance of KTO NBs, leading to the rapid diffusion and intercalation of potassium ions in KTO NBs. In addition to improving the conductivity of graphene nanosheets, this braided structure also facilitates the penetration of electrolyte ions, shortens the diffusion distance, and accelerates reaction kinetics. It can provide excellent specific capacity and rate performance ( $87 \text{ mAh g}^{-1}$  at  $1 \text{ A g}^{-1}$ ) and the stability of ALD KTO, which also benefits from the solid solution potassium mechanism.

### 3.1.3. Soft carbon

Soft carbon is a kind of graphitized material, the graphitization degree of which can be adjusted by annealing, and at  $2600^\circ\text{C}$  into graphite. Soft carbon has a turbine-layered carbon lattice structure with strong structural flexibility, so its layer spacing is controllable. Reasonable layer spacing is conducive to improving the ionic conductivity of the material. Meanwhile, the defects on the surface of soft carbon can be used as the active site for ion storage, which improves the material's dynamic and rate performance.

The central carbon sources used in the soft carbon anode are petroleum pitch, mesophase pitch, coal liquefaction residue, etc. The asphaltene component in petroleum pitch is typically rich in deposited metal ions, which are transformed into a metal-nitrogen-carbon structure during carbonization. This transformation weakens the adsorption of potassium ions. Therefore, investigating the impact of asphaltene components found in petroleum pitch on enhancing the capabilities of carbon materials in potassium-ion capacitors is a crucial area of research. Soft carbon nanosheets (SCNs) were synthesized using NaCl templates through the pyrolysis of petroleum pitch, as shown in Figure 4(a).<sup>[43]</sup> HRTEM images indicate that SCNs have a typical amorphous structure with a layer spacing of 0.396 nm, which enables a reversible  $\text{K}^+$  insertion/extraction process. The disordered carbon layers exhibit high structural elasticity, allowing them to accommodate mechanical deformation during potassium conversion and distribute active sites for  $\text{K}^+$  storage. The SCNs electrode delivers a capacity of  $240.5 \text{ mAh g}^{-1}$  (Figure 4b). Besides, Wang et al. prepared coal pitch-derived carbon nanofibers precursors using a facile electrostatic spinning technique.<sup>[44]</sup> The precursors were then carbonized and activated with KOH to synthesize fibrous carbon materials and fabricate dual-carbon PIHCs as the anode (PCNF) and cathode (aPCNF) electrodes, respectively (Figure 4c and d). By employing appropriate micro/mesoporous structures, continuous three-dimensional conductive networks, patterned crystallites, and increased surface pseudo-capacitance, the constructed PIHCs (PCNF//aPCNF) exhibit excellent energy density, attractive

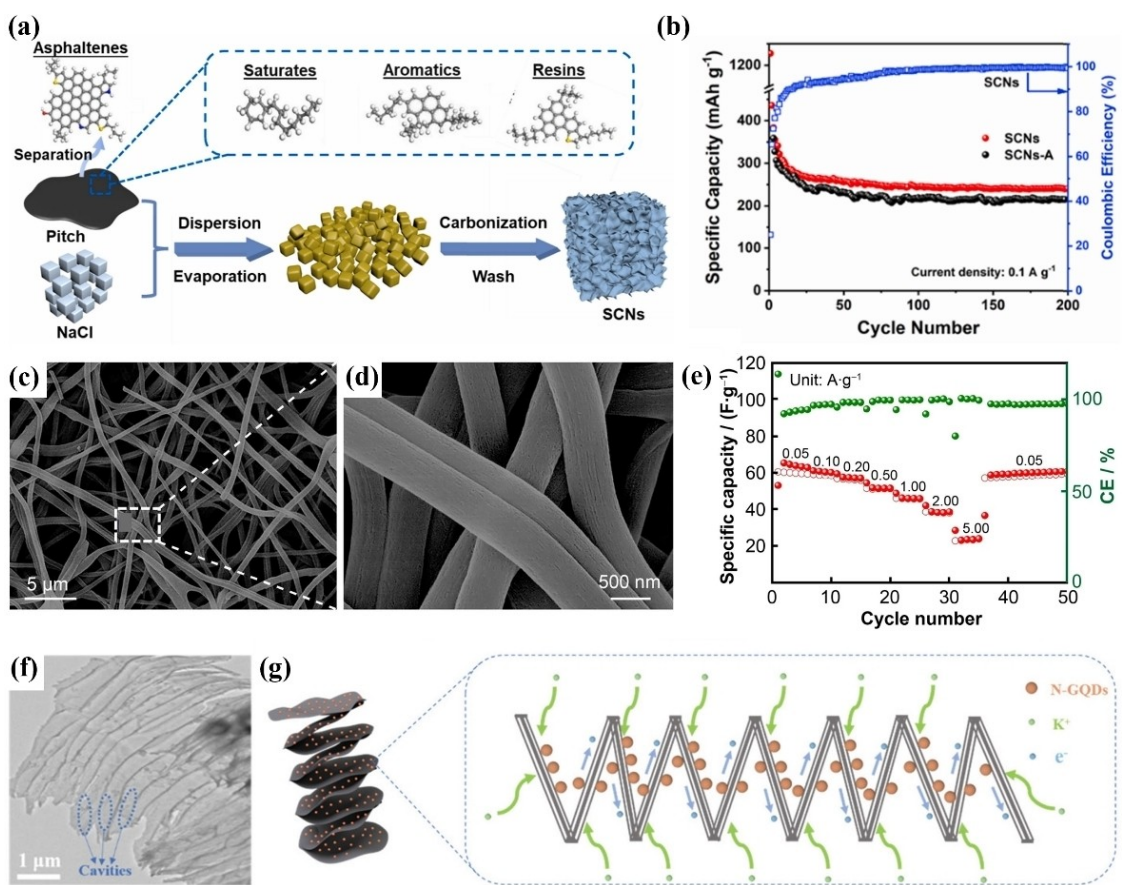


**Figure 4.** a) Schematic illustration of the preparation of SCNs. b) Cycling properties of SCNs at  $0.1 \text{ A g}^{-1}$ . Reproduced with permission from Ref. [43]. Copyright (2022) Elsevier. c and d) FESEM images of PCNF. e) Rate performance of the PIHCs (PCNF//aPCNF). Reproduced with permission from Ref. [44]. Copyright (2022) Wiley-VCH. f) SEM images and g) schematic illustration of potassium-ion storage mechanism of N-GQD@ASC-500. Reproduced with permission from Ref. [45]. Copyright (2021) Wiley-VCH.

capacity retention and low leakage current, and average self-discharge capability (Figure 4e).

The available active sites of  $\text{K}^+$  on the soft carbon are limited, and the diffusion path of  $\text{K}^+$  is blocked by the film covering the soft carbon micro rods. Zhang et al. proposed an oxidation method to remove the skin-like carbon film by selectively etching PTCDA-derived soft carbon micro rods and constructing a novel accordion-like layered structure with a layered micro-meso-macroporous carbon framework, facilitating potassium ions to insert/desert through the channel conveniently and provides ample ion storage sites (Figure 4f).<sup>[45]</sup> The novelty of this study lies in the existence of many accordion-shaped voids between the soft carbon nanosheets. The use of nitrogen-doped graphene quantum dots on soft carbon nanosheets results in a larger electrode-electrolyte contact area, shorter diffusion distance, stable buffer volume expansion during insertion/extraction, and improved cycling stability. This also enhances the adsorption capacity of potassium ions, conductivity, and wettability, as shown in Figure 4(g). Notably, the N-6 content achieved through annealing treatment significantly improves the reversible storage capacity.

### 3.1.4. Hard carbon

Hard carbons (HCs) are a type of carbon resistant to carbonization even at temperatures as high as  $2800^\circ\text{C}$ . This resistance is due to the difficulty of rearranging the carbon atoms to form an ideal layered structure at such high temperatures. As a result, the internal structure of HC is destroyed, forming many pores, which increases the specific capacity to a certain extent. The disordered structure and large interlayer spacing of HC make it easier for large alkali metal ions such as  $\text{Na}^+$  and  $\text{K}^+$  to be inserted and extracted. HC have better potassium storage capacity but lower energy density and ICE than soft carbons. Therefore, modification of HC by different methods is the leading work. Li's work clarified two different potassium storage mechanisms in HC, including i) adsorption onto defect-/edge-sites and micropores at high voltage region and ii) intercalation into graphite layer at low voltage region (Figure 5a and b).<sup>[46]</sup>

Sufficient micropores act as active sites for efficient potassium storage and ion buffer pools, which relieve volume expansion and ensure high specific volume and good structural stability. In addition, the abundant mesopores in the porous structure provide conductive pathways for ion diffusion and electrolyte permeation, enabling fast ion/electron transport

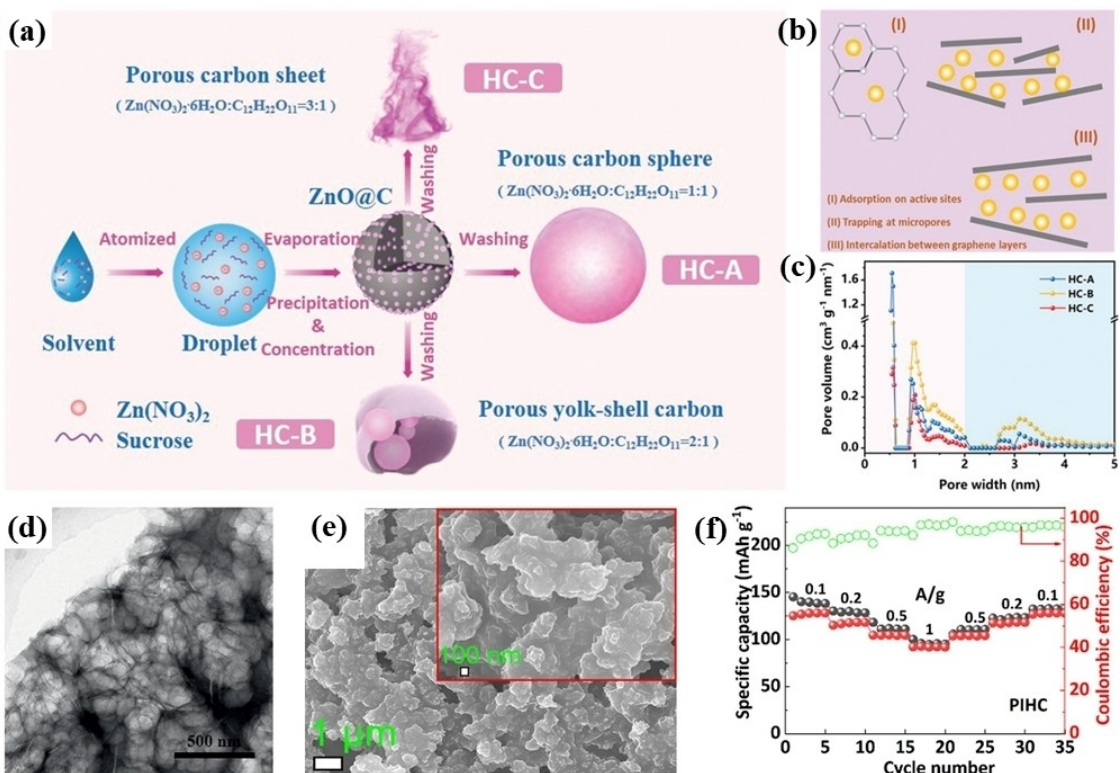


**Figure 5.** a) Schematic illustration of the preparation process for the HC–X (X=A, B, C) samples. b) Schematic illustration of potassium-ions storage mechanism in HCs. c) BJH (Barrett-Joyner-Halenda) pore size distribution plots of the HC–X. Reproduced with permission from Ref. [46]. Copyright (2021) Wiley-VCH. d) TEM image of the carbon foam. Reproduced with permission from Ref. [47]. Copyright (2020) Elsevier. e) SEM image of PNTCDA. f) Rate property of PIHCs (PNTCDA@900//AC) from 0.1 to 1 A g<sup>-1</sup>. Reproduced with permission from Ref. [48]. Copyright (2020) Elsevier.

kinetics (Figure 5c). The carbon foam prepared by Feng et al. contains abundant micropores, providing a channel for the penetration of anions and cations and reducing the graphite layer's volume expansion (Figure 5d).<sup>[47]</sup> Liu et al. synthesized PNTCDA, a polyimide-inspired volcanic rock-like carbon material, which exhibits promising applications due to its N/O doping, mesoporous construction, abundant active sites, and strong capacitance effect (Figure 5e).<sup>[48]</sup> PNTCDA@900 displays stable cyclability and excellent rate cyclability (Figure 5f). Besides, the wing-like porous carbon sheets (WPCSSs) were assembled by numerous interconnected hollow carbon bubbles with a high SSA of 1261 m<sup>2</sup> g<sup>-1</sup>.<sup>[49]</sup> The as-prepared WPCSSs materials benefited from a multilayer porous structure, high SSA, and oxygen-rich functional groups. Recently, Liu et al. prepared porous carbon with Russian-doll-like pores pre-intercalated with K<sup>+</sup> through an ebullient carbonization process.<sup>[50]</sup> The main internal factor is that the alkali can penetrate the three-dimensional space of dihydrazine malonate layer by layer. The confinement effect forms deep pore structures of different dimensions. K<sup>+</sup>-pre-intercalated porous carbon with Russian-doll-like pores (KPCRPs) anode material has an open structure and sizeable interlayer spacing with a larger surface area of 1181.32 m<sup>2</sup> g<sup>-1</sup> and a higher pore volume (1.23 cm<sup>3</sup> g<sup>-1</sup>). The total pore volume comprises 62.3% micropores and 36.9% mesopores/macropores, indicating a multimodal pore architecture. Mesopores serve as active sites that enhance the platform capacity,

facilitate ion migration, and stabilize carbon during the (de)potassium process. Micropores contribute to effective adsorption, while mesopores are closely associated with intercalation contribution capacity and ICE.

Materials with specific structures greatly influence the overall performance of PIHCs. Inspired by bubble wraps, the bubble-wrap-like carbon sheet (BPCS) with rigid-flexible coupled microscale porous structure has been fabricated with solid structural stability and reasonable volume expansion control (Figure 6a).<sup>[51]</sup> A K<sub>2</sub>CO<sub>3</sub>·1.5H<sub>2</sub>O-dominated SEI film is generated, in which these grains form a more stable framework and more K<sup>+</sup> transport channels, significantly improving the SEI function. The assembled BPCS//NPC (N-doped porous carbon) PIHCs exhibit a high energy density even at 10 A g<sup>-1</sup> after 5000 cycles (Figure 6b). Wang's team synthesized the bead-like coal-derived carbon films (BCCFs) by electro-spinning and carbonization (Figure 6c).<sup>[52]</sup> On the one hand, the bead-like structure provides a three-dimensional network of carbon fiber structures with numerous electron/ion transport channels and excellent strength (Figure 6d). On the other hand, carbon particles derived from coal possess spherical active sites and have a high ratio of nitrogen- and oxygen-containing functional groups. These functional groups create ample interfaces for the adsorption of potassium ions, thereby enhancing the transportation of electrolytes and ions.

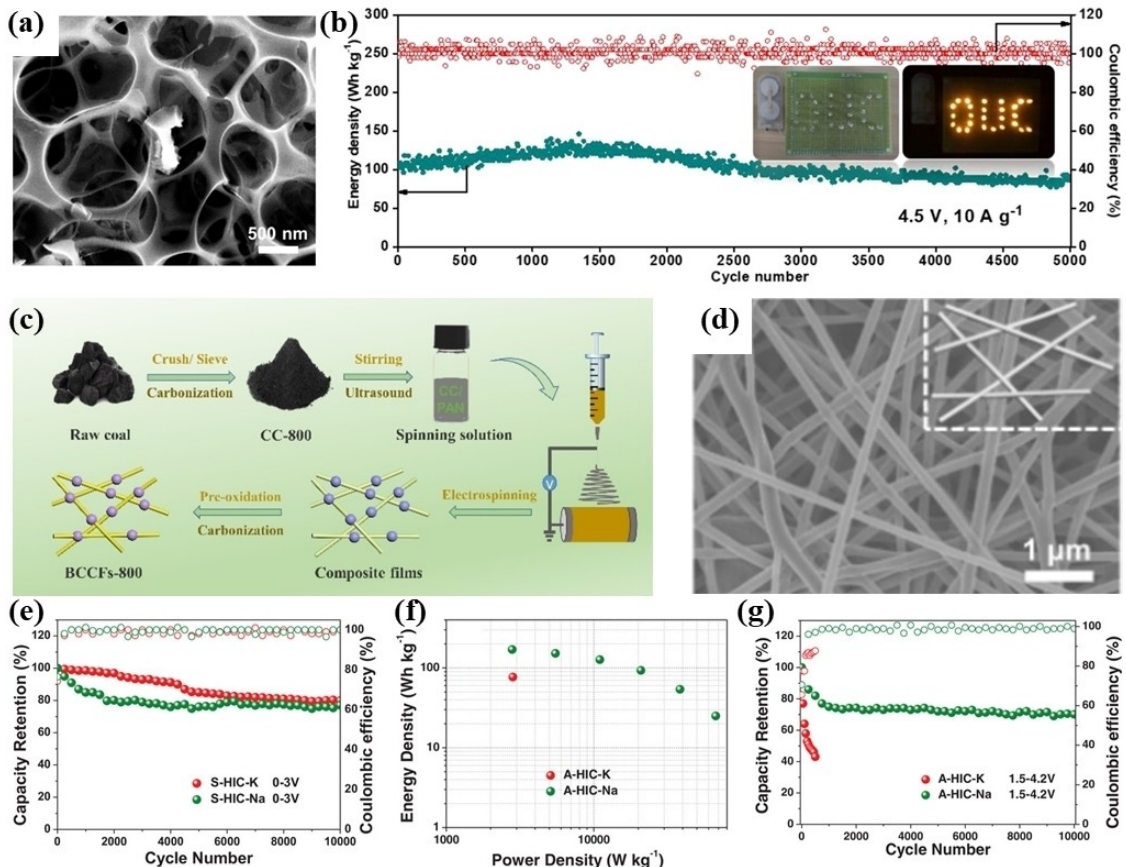


**Figure 6.** a) SEM image of the inner structure of BPCS. b) The cycling performance of the PIHCs (BPCS/NPC) was tested at  $10 \text{ A g}^{-1}$ . Reproduced with permission from Ref. [51]. Copyright (2020) American Chemical Society. c) Schematic illustration of the preparation process for BCCFs-800. d) SEM image of BCCFs-800. Reproduced with permission from Ref. [52]. Copyright (2022) Wiley-VCH. e) Cycling performance of symmetric PIHCs and sodium ion hybrid capacitors (SIHCs) tested at  $0.8 \text{ A g}^{-1}$ . f) Ragone plot comparison, and g) cycling performance of asymmetric PIHCs and SIHCs. Reproduced with permission from Ref. [54]. Copyright (2019) Wiley-VCH.

**Biomass-derived carbon:** Biomass materials usually exhibit a wide variety of macrostructures. The derived carbon is amorphous, composed of randomly distributed small graphitized fragments and hierarchical pore structure.<sup>[53]</sup> It has the advantages of fine hierarchical structure, excellent surface electrochemical activity, and electrical conductivity, and it is environmentally friendly and low-cost. Two types of natural precursor-derived materials were developed by Xu et al.<sup>[54]</sup> The first type is a dense, hard carbon from leftover silkworm feed, specifically mulberry tree stems. The second type is an N-rich carbon derived from silkworm waste, which has high SSA ( $1602 \text{ m}^2 \text{ g}^{-1}$ ) and abundant nitrogen and oxygen content (11.7 and 16.9 wt%). Symmetric PIHCs and asymmetric PIHCs were assembled to test the electrochemical performance (Figure 6e and g). The symmetric PIHCs achieve  $51 \text{ Wh kg}^{-1}$  at  $1260 \text{ W kg}^{-1}$  and have long-term cycling stability (10,000 cycles), while asymmetric PIHCs yield  $77 \text{ Wh kg}^{-1}$  at  $2830 \text{ W kg}^{-1}$  but cycle quite poorly (less than 1,000 cycles) (Figure 6f). This may be a direct result of the low rate capability of the hard carbon anode, which cannot (de)potassium even at  $0.4 \text{ A g}^{-1}$ . In the initial phase of the cycle, the hard carbon traps potassium ions, which hinders further charging and discharging processes. Chen et al. also used silkworm excrement as a precursor to prepare AC.<sup>[55]</sup>

After the graphene solution was fed to the silkworms, the excrement collected was processed through salt activating to produce the N-rich carbon/graphene composite (SEG). AC without graphene (SE) was used as a comparison sample. The specific capacity of AC decreases only slightly at higher current densities due to its particular hollow particle structure and heteroatom doping. The capacity of SEG is further improved with the addition of graphene. Even at  $80 \text{ A g}^{-1}$ , SE and SEG exhibit high capacitances of  $164$  and  $187 \text{ F g}^{-1}$ , respectively. It is the reason that the rich pore structure and smooth surface in carbon materials enhance the accessibility of electrolytes into the microporous regions, thus still providing fast ion transfer pathways at increased current densities.

The electrochemical properties of materials can be enhanced by modifying defects and pore size. Qian et al. utilized high-temperature hydrothermal ‘disproportionation’ of basswood to prepare dual-carbon PIHCs with an oriented carbon microspheres (OCMSs) anode and 3D porous carbon (3DPC) cathode (Figure 7a).<sup>[56]</sup> This approach created a unique anode-cathode system that exhibited improved electrochemical properties. The organic components were produced by the successive decomposition of hemicellulose, cellulose, and lignin from the basswood block during a high-temperature hydro-

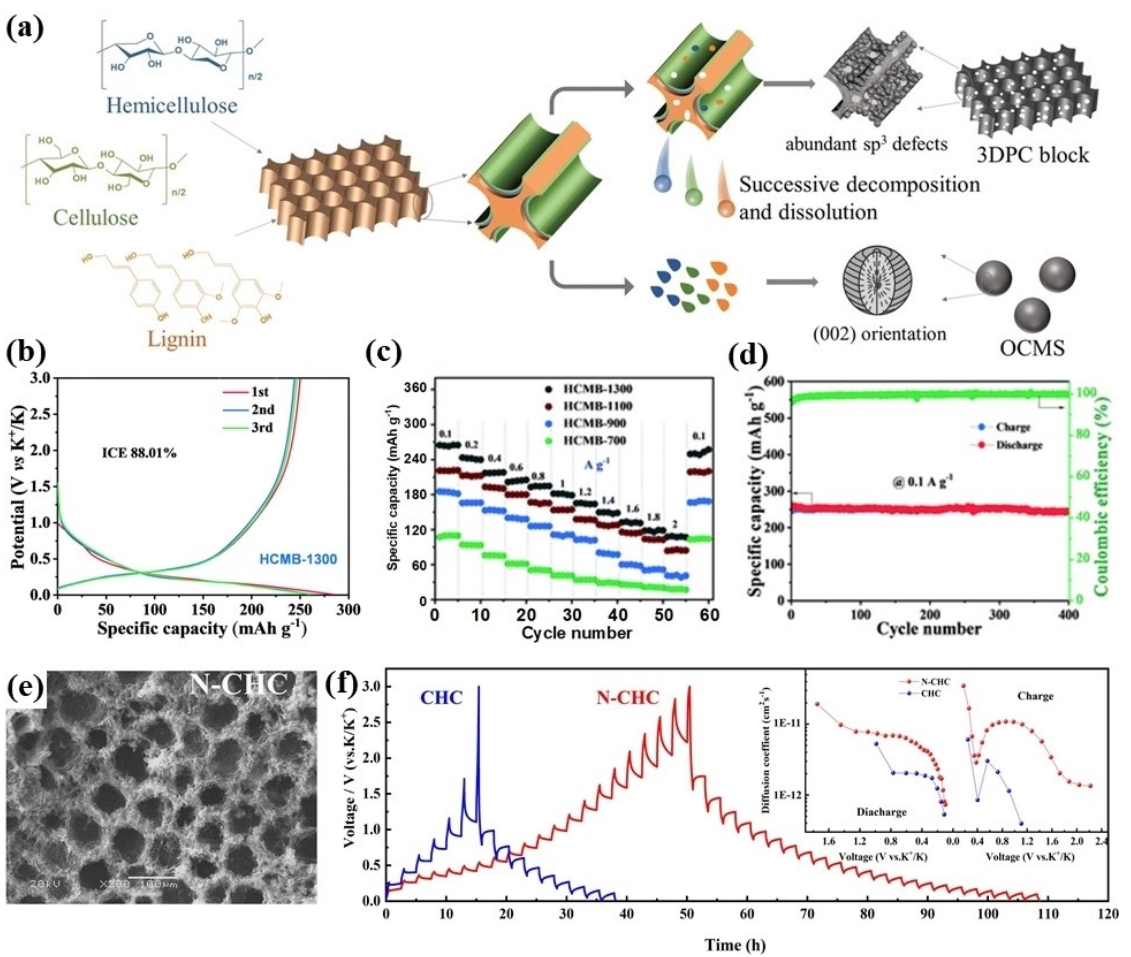


**Figure 7.** a) Schematic illustration of the formation mechanism for OCMS and 3DPC. Reproduced with permission from Ref. [56]. Copyright (2021) Wiley-VCH. b) Galvanostatic charge-discharge (GCD) curves of HCMB-1300 electrodes. c) The rate capability of HCMB-700, HCMB-900, HCMB-1100, and HCMB-1300 in half-cells. d) Cycling stability of HCMB-1300 at 100 mA g<sup>-1</sup>. Reproduced with permission from Ref. [57]. Copyright (2022) Royal Society of Chemistry. e) SEM image of N-CHC. f) GITT tests and diffusion coefficient of N-CHC and CHC. Reproduced with permission from Ref. [58]. Copyright (2021) Elsevier.

thermal process. These components were then dissolved in water and carbonized into OCMSs. The remaining organic matter is converted into 3DPC blocks rich in  $sp^3$  defects and large quantities of micropores. Recently, a self-supporting hard carbon microbelt (HCMB) film was developed using precursor-sanitary tissue and carbonization.<sup>[57]</sup> In their analysis, the researchers examined the effect of carbonization temperature on the structure of the material and its ability to store K<sup>+</sup>. They observed that as the temperature increased, the microstructure of carbon in HCMB transitioned from a short-range open disorder to a long-range closed disorder. Interestingly, HCMB-1300 exhibited unexpectedly high ICE (88%) and demonstrated better electrochemical performance compared to the other samples (Figure 7b-d). A high carbonization temperature favors the formation of a closed, randomly oriented turbine layered structure, resulting in more ribbons of graphite crystallites with fewer defects. These curved carbon layers and closed nanopores can provide more active potassium storage sites, resulting in higher platform capacity.

The addition of heteroatoms to biomass has been found to increase active sites and improve carbon material properties.

Wang et al. utilized hemp core as the raw material and urea as the etchant to fabricate a nitrogen-rich biomass carbon (N-CHC). The resulting material exhibited a high SSA of  $1185.3\text{ m}^2\text{ g}^{-1}$  and an N content of 8.56% (Figure 7e).<sup>[58]</sup> During the process of pyrolysis, urea produces isocyanic acid, a highly corrosive substance that affects lignin and hemicellulose. Additionally, ammonia is also produced during pyrolysis and can modify the structure of graphite layers, increasing the number of heteroatoms. The process of N-doping results in a faster electrochemical reaction rate for N-CHC (Figure 7f). The PIHCs (N-CHC//AC) exhibit a maximum energy density of  $127.36\text{ Wh kg}^{-1}$  and a maximum power density of  $2371\text{ W kg}^{-1}$ . Fucoidan, a concentrated pyrosulfated polysaccharide derived from seaweed, is composed of a carbon chain structure and contains numerous sulfate and hydroxyl groups. These properties make it a promising source of carbon precursors. A NaCl template was used to synthesize a fucoidan-derived oxygen-rich carbon nanosheet (FOCN) material.<sup>[59]</sup> A competitive capacity of  $392\text{ mAh g}^{-1}$  was achieved at  $0.05\text{ A g}^{-1}$  due to its porous 2D foil structure, abundant oxygen doping, and expanded graphite layer in the amorphous structure. Cai et al.

obtained S-doped carbon materials (S–Cs) by doping commercially procured sulfur with corn, soybeans, batam, and shallot, respectively, and annealed at high temperatures.<sup>[60]</sup> The yield of aromatic carbon generated by carbonization increases and more potassium ions can be introduced. In addition, sulfur can be doped onto  $sp^3$  hybridized carbons close to the arene ring. The carbons with pseudocapacitive sites are difficult to separate from the substrate and destroy the arene-conjugated planar structure.

**MOFs:** Metal-organic frameworks (MOFs) are crystalline porous materials in which abundant metal-centric ions and organic ligands show the advantages of structure and composition diversity, high porosity, large SSA, good thermal stability, ordered crystal structure, and low density.<sup>[61,62]</sup> A porous carbon microsheet anode (MDPC) was created through the thermal transformation of sheet-like manganese-based MOFs. The resulting MDPC had a disordered, interlayer-expanded, oxygen-doped structure that was 100–300 nm thick and 1–3  $\mu\text{m}$  long (Figure 8a).<sup>[63]</sup> By utilizing the MDPC electrode as an anode and combining it with a home-made porous carbon (PDPC) as the cathode, the PIHCs are capable of delivering a remarkable operational working voltage of 4.2 V and an energy density of 120  $\text{Wh kg}^{-1}$  (Figure 8b). Besides, a core-shell heterostructure ( $\text{TiO}_2/\text{C}@\text{NPSC}$ ) was created by pyrolyzing a MIL-125 (Ti) MOFs precursor modified by a PZS polymer. The resulting structure is

a titanium oxide/carbon nanocomposite confined into N, P, and S co-doped carbon (Figure 8c).<sup>[64]</sup> The  $\text{TiO}_2/\text{C}@\text{NPSC}$  structure resembles a dragon fruit, with  $\text{TiO}_2$  nanoparticles evenly dispersed throughout the porous carbon matrix. This matrix is derived from the organic components of the MOFs and retains the original tablet-like framework of the MOFs precursor. Additionally, a protective shell of N, P, and S co-doped carbon derived from the PZS polymer covers the surface of the  $\text{TiO}_2/\text{C}$  particle. The PIHCs device, which couples  $\text{TiO}_2/\text{C}@\text{NPSC-700}$  as the anode and AC derived from another MOFs precursor of ZIF-8 as the cathode, achieves high energy-power characteristics (max energy density = 114  $\text{Wh kg}^{-1}$ , max power density = 21  $\text{kW kg}^{-1}$ ) and excellent stability (10 000 cycles).

**Heteroatom-doped carbon:** Heteroatom doping is an effective way to adjust the electronic properties of carbonaceous materials and increase the interlayer spacing, speeding up the ion diffusion rate and leading to high  $\text{K}^+$  storage performance.<sup>[65–67]</sup> Nitrogen atom has a small atomic radius and high electronegativity, and the doping method is relatively simple. Therefore, the most common type of single-element doping is nitrogen doping.<sup>[68,69]</sup> The doped nitrogen atoms are present in carbon materials in different configurations, such as forming pyridine-N, pyrrole-N, graphite-N, and pyridine nitrogen oxides.<sup>[70]</sup>

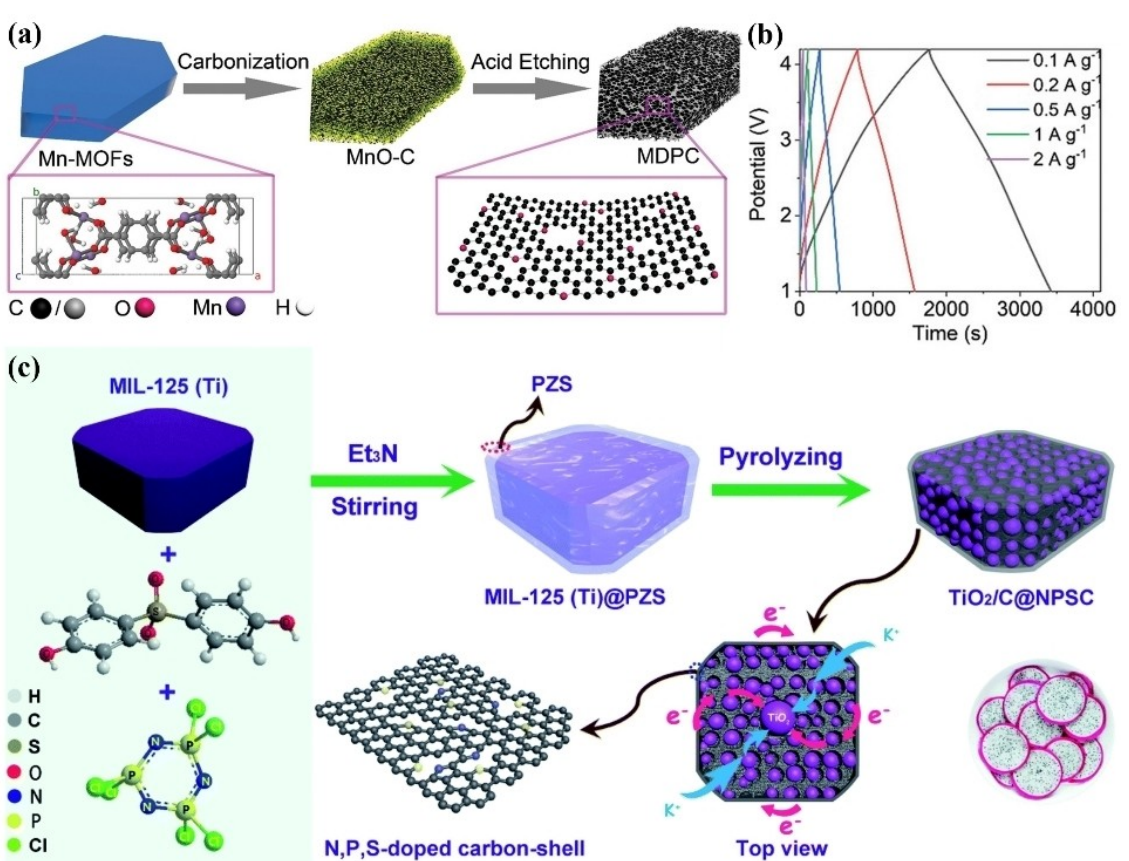


**Figure 8.** a) Synthetic procedures of MDPC. b) charging/discharging curves of the PIHCs (MDPC//PDPC) at different current densities. Reproduced with permission from Ref. [63]. Copyright (2020) Wiley-VCH. c) Schematic illustration of the preparation process and the structural characteristics of  $\text{TiO}_2/\text{C}@\text{NPSC}$ . Reproduced with permission from Ref. [64]. Copyright (2020) Royal Society of Chemistry.

Since the valence electron layer of the nitrogen atom is one more electron than the carbon atom, the nitrogen atom can be used as an electron donor to improve the conductivity of N-doped carbon materials. In addition, the electronegativity difference between N and C can improve the wettability of the material, which can make the electrode and electrolyte fully contact. Qiu et al. fabricated the nitrogen-doped hierarchical porous hollow carbon spheres (NHCS) (uniform size  $\approx$  330 nm) (Figure 9a and b). Based on the kinetic analysis and density functional theory calculations, it has been revealed that the energy storage mechanism of NHCS is predominantly driven by the capacitive behavior of nitrogen atoms and the hierarchical pore structure.<sup>[71]</sup> Similarly, a kind of hollow carbon nanospheres (NHCNs) were obtained with similar structure but a smaller size ( $\approx$  160 nm) (Figure 9c). They investigated the influence of different shell thicknesses on potassium storage properties. When the shell thickness is 20 nm, the electrochemical performance of the NHCNs is the best. Besides, Liu et al. also fabricated a kind of nitrogen-doped porous carbon submicrospheres (NCP)

as an anode for potassium storage derived from micro-flower-like polyimide superstructure (Figure 9d).<sup>[73]</sup> The microsphere constructed from two-dimensional carbon nanosheets had a diameter of approximately 600–800 nm and a thickness of approximately 25 nm. Yang et al. were able to synthesize a three-dimensional (3D) nitrogen-doped framework carbon (3DNFC) with a high nitrogen-doping (5.74 at%) through the simple calcination of EDTA-4Na without the need for any additional nitrogen source, template, or catalyst.<sup>[74]</sup> Nitrogen doping widens the interlayer spacing, resulting in random combinations of graphite and turbine layer stacks and ease of inserting potassium ions into the layered structure (Figure 9e). The dual-carbon PIHCs (3DNFC//3DNFAC) could typically work at 0–4.2 V (Figure 9f) and deliver high energy and power densities. Similarly, a self-template method was utilized to prepare an N-doped amorphous porous carbon with a 3D network structure (NPC).<sup>[75]</sup> This structure facilitates fast electron transfer channels. The high N-doping level (5.84 at%) also

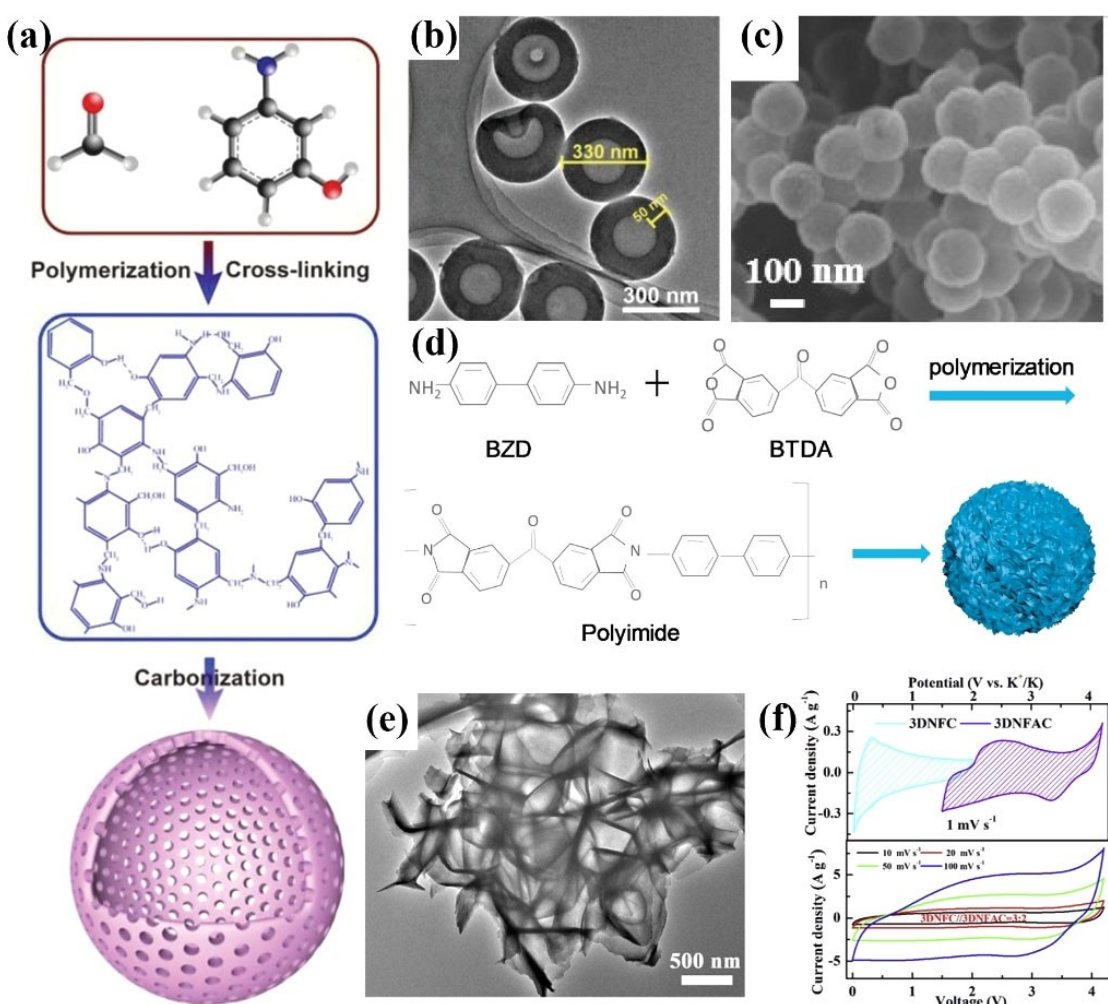


**Figure 9.** a) Schematic illustration of the preparation process for NHCS. b) HRTEM image of NHCS. Reproduced with permission from Ref. [71]. Copyright (2019) Wiley-VCH. c) SEM image of NHCNs-420. Reproduced with permission from Ref. [72]. Copyright (2022) Elsevier. d) Schematics of the synthesis protocol for NCP. Reproduced with permission from Ref. [73]. Copyright (2020) Elsevier. e) TEM image of 3DNFC. f) CV curves of 3DNFC and 3DNFAC in a K half-cell at a scan rate of 1 mV s<sup>-1</sup> (top), CV curves of PIHCs (3DNFC//3DNFAC) with the mass ratio of 3:2 at different scan rates (bottom). Reproduced with permission from Ref. [74]. Copyright (2019) Elsevier.

enhances conductivity and increases the number of structural defects in the carbon-active host materials.

Therefore, it can be found that the doping of nitrogen atom: 1) Expands the layer spacing and reduces the energy barrier of potassium ion embedding. 2) Generates more defects in carbon materials and adds more active sites. 3) Increases the SSA, thus improving the wettability between electrode and electrolyte. However, high SSA tends to consume large amounts of electrolytes to form SEI layers, resulting in low ICE. 4) Adjusts the distribution of electrons near carbon atoms to enhance the electron conductivity. Therefore, introducing nitrogen atoms ensures fast kinetics and structural stability during cycling to a certain extent, thus making it show excellent energy and power density when assembled into PHCs.

The co-doping of multiple elements can significantly improve the properties of materials, mainly attributed to heteroatoms' synergistic action.<sup>[76]</sup> Compared with single-element doping, co-doping can produce more defects and active sites, increase layer spacing, and further optimize the distribution of electrons around carbon atoms to improve the conductivity of materials.<sup>[77,78]</sup>

Common forms of co-doping are mostly double-element co-doping, such as N/P co-doping, N/S co-doping, and N/O co-doping, while co-doping containing three or four elements is relatively rare.<sup>[79]</sup> Wang et al. utilized a supramolecular assembly-directed one-pot strategy to produce hierarchical porous P/N co-doped pancake-like carbon (PN-PanC) with atomic percentages of 93.6% C, 1.6% P, and 4.9% N (Figure 10a).<sup>[80]</sup> Their findings indicate that P/N co-doping can effectively regulate the electronic structure of the material and manipulate the

adsorption kinetics of both anions and cations, as supported by density functional theory (DFT) calculations. Compared to sheet structure, a self-sacrifice template strategy was used to synthesize N/P-doped network porous carbon materials (NPMCs), which possess abundant hierarchical pores, larger interlayer spacing, and high SSA and abundant defects (Figure 10b).<sup>[81]</sup> The simulation results indicate that the adsorption energy of potassium ions on N/P-doped carbon is significantly lower compared to that of single-element doped or undoped carbon, which means that it is more thermodynamically conducive to the adsorption of potassium ions on the electrode (Figure 10c). In addition, introducing N/P atoms results in a localized increase in electron density, which works in conjunction with vacancies to enhance the transfer of charges between potassium atoms. Recently, Gao et al. successfully produced phosphorus and nitrogen dual-doped hollow carbon spheres (PNHCS) using a nanoscale-confined *in situ* polymerization process. The PNHCS exhibited superior cycling and rate performance compared to the solo N-doping sample (NHCS).<sup>[82]</sup> With the introduction of P, the content of pyridine-N increases from 16.8% in NHCS to 32.9% in PNHCS, which is attributed to more open-edge sites and defects generated by P-doping. DFT results indicate that P-doping with more pyridine-N groups is beneficial to the kinetic process of electron and potassium ion transfer.

N/S co-doping is also a standard method in the modification of carbon materials.<sup>[83]</sup> Compared to nitrogen, sulfur has a relatively larger size but lower electronegativity. This property can significantly expand the distance between carbon layers, allowing for the embedding of potassium ions.<sup>[84,85]</sup> Hu et al.

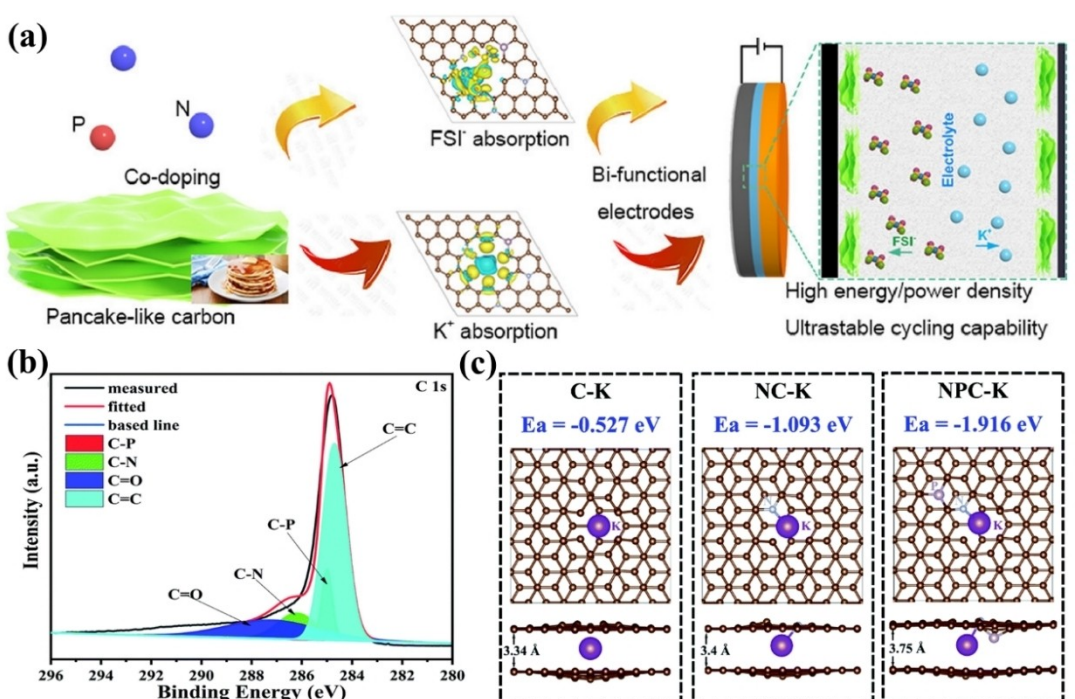


**Figure 10.** a) The illustration of the formation process of PN-PanC. Reproduced with permission from Ref. [80]. Copyright (2022) Elsevier. b) C 1s spectrum of NPMC-700. c) Top and side illustration of simulations for one K<sup>+</sup> ion absorbed on C-K, NC-K, and NPC-K. Reproduced with permission from Ref. [81]. Copyright (2022) Royal Society of Chemistry.

reported N/S co-doped porous carbon nanosheets (S-N-PCNs).<sup>[86]</sup> The pyridine-N content of N-PCN increased from 33.8% to 52.9% of S-N-PCN after doping with additional sulfur atoms, suggesting that the addition of sulfur has been shown to enhance the formation of carbon materials with high pyridinium content. Research has demonstrated that an increased proportion of pyridine-N in these materials can significantly enhance their ability to store potassium ions and facilitate electron transfer, ultimately leading to improved potassium storage performance. (Figure 11a–c). Fan et al. created N/S dual-doped carbon (N, S-3DHPC-600) with a 3D hierarchical porous structure and compared it to single element doped or undoped samples (Figure 11d).<sup>[87]</sup> Their findings showed that the synergistic effect of N and S can accelerate the formation of a complete SEI layer, leading to an improvement in ICE. The Coulombic Efficiency (CE) of both S-3DHPC and N, S-3DHPC-600 electrodes reaches nearly 90% after 6 cycles, which is higher compared to the other two electrodes. It underscores the significance of S-doping in improving CE (Figure 11e).

What is more, N/O co-doping is also a form of heteroatom doping. Peng et al. synthesized NO-doped carbon nanosheets (NOCSs) with a hierarchically porous structure, large interlayer

spacing, disordered structure, and sufficient pyridinic-N functional groups (Figure 11f).<sup>[88]</sup> The presence of abundant active N/O functional groups enhances ion diffusion, electrolyte penetration, and charge transfer. The multiple functional groups also provide numerous active sites for potassium storage. In addition, N-6 and N-5 contribute more to improving potassium storage than N-Q. By annealing, Dou et al. synthesized N/O co-doped porous carbon spheres (PCSs).<sup>[92]</sup> Oxygen-containing functional groups can promote the wettability of the porous carbon surface and contribute to electrolyte penetration, which allows rapid electrolyte penetration through the entire electrode to achieve rapid ion diffusion, resulting in faster kinetics and full utilization of the active material. Profited from the abundant mesoporous structure and N/O doping, the PCSs anode shows high storage capacity ( $413.5 \text{ mAh g}^{-1}$ ) and ultra-long-term cycling stability (over 40,000 cycles at  $5 \text{ Ag}^{-1}$ ). P/O dual-doped porous carbon spheres (P/O-PCSs) were synthesized by Zhao et al. (Figure 12a).<sup>[89]</sup> Previous work has mentioned that incorporating potassium ions into hard carbon leads to an irreversible rearrangement of the carbon layer and accumulates nearby parts of graphite.<sup>[93]</sup> However, some potassium ions are preferentially adsorbed on the introduced P/O functional

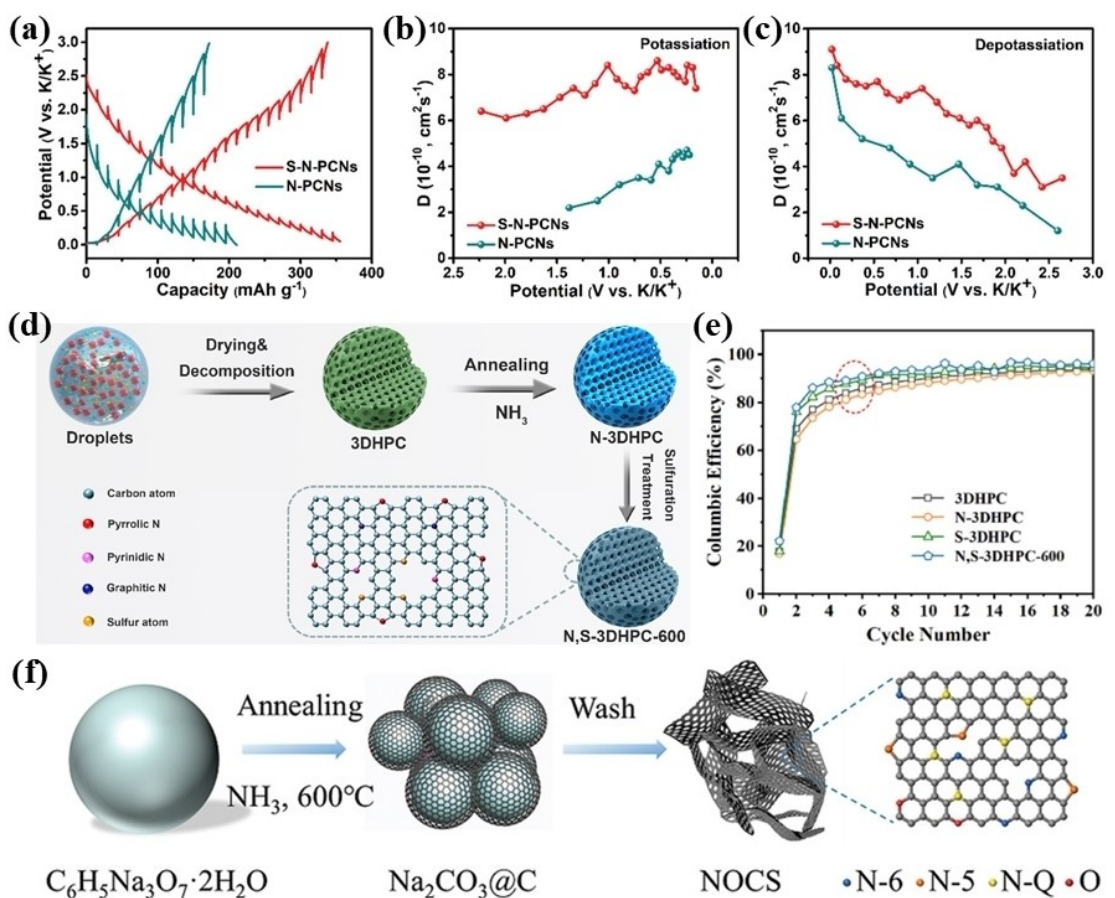


**Figure 11.** a) GITT curves of S-N-PCNs and N-PCNs at the 100th cycle. b, c) The K-ion diffusion coefficient of S-N-PCNs and N-PCNs was obtained via the GITT technique during potassiation and depotassiation. Reproduced with permission from Ref. [86]. Copyright (2019) Wiley-VCH. d) Schematic illustration of N,S-3DHPC-600 and structure characterizations of N,S-3DHPC-600. e) Coulombic efficiencies of 3DHPC, N-3DHPC, S-3DHPC and N,S-3DHPC-600 electrodes. Reproduced with permission from Ref. [87]. Copyright (2020) Elsevier. f) Schematic illustration of the preparation process for NOCSs. Reproduced with permission from Ref. [88]. Copyright (2020) Wiley-VCH.

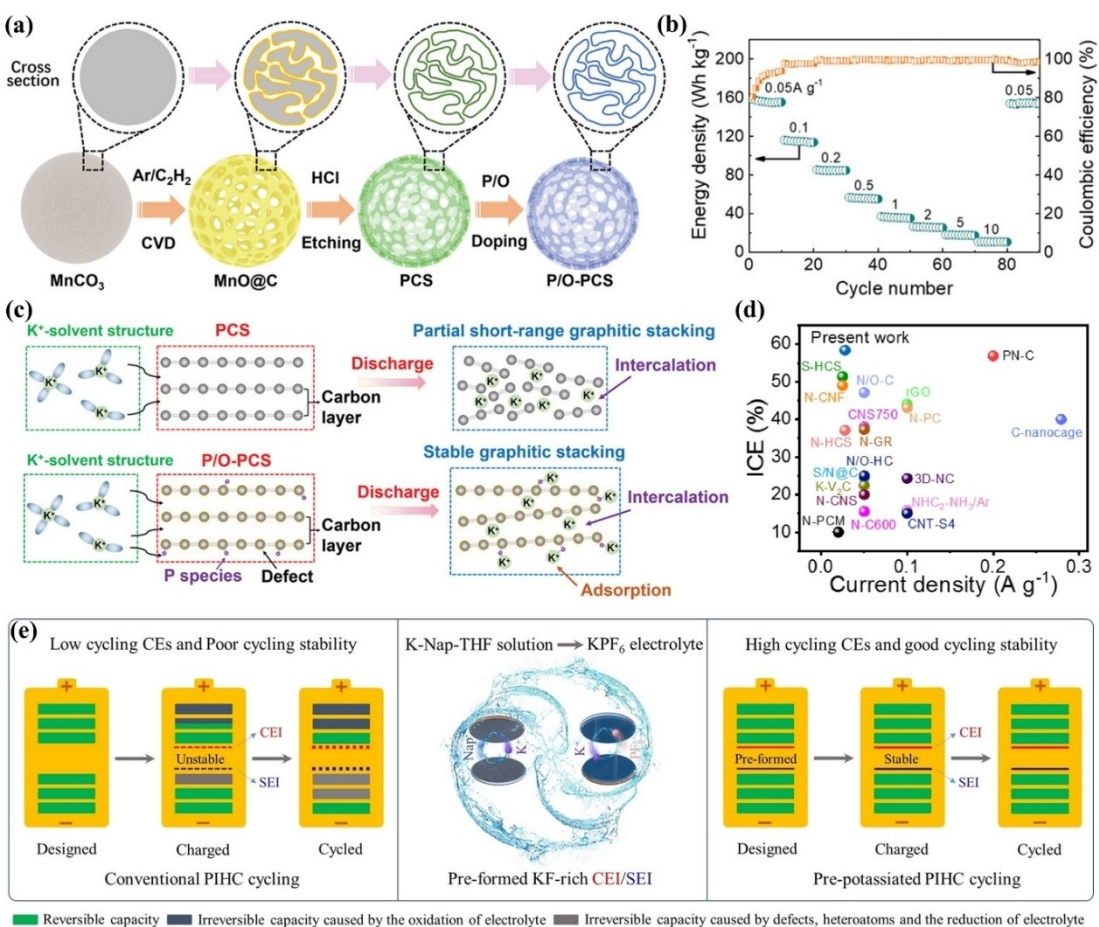


**Figure 12.** a) The synthesis process of P/O-PCS. b) Rate performance of the PIHCs (P/O-PCS//AC) (0.05 to 10 A g<sup>-1</sup>). c) Scheme of the P/O dual doping strategy concerning the potassium storage mechanism. Reproduced with permission from Ref. [89]. Copyright (2021) Wiley-VCH. d) Comparison of ICE between MHC and other carbon materials as an anode in PIBs. Reproduced with permission from Ref. [90]. Copyright (2021) Elsevier. e) Schematic illustration of the pre-potassiation process and its effects on dual-carbon PIHCs. Reproduced with permission from Ref. [91]. Copyright (2023) Wiley-VCH.

groups after modification, forming a “buffer zone”. This reduces the number of potassium ions embedded in the carbon layer, avoids further structural decomposition, and largely alleviates the irreversible transformation (Figure 12c). Thus, the reversible potassium uptake mechanism is kinetically faster and less disruptive than the conventional intercalation behavior. Dubal et al. turned waste textiles into N/S/O-doped hard carbon (MHC) with large interlayer spacing.<sup>[90]</sup> As shown in Figure 12(d), the ICE (58.4%) for the MHC electrode is significantly improved, which can be attributed to the multi-heteroatom doping and low SSA, thus significantly reducing the irreversible reactions and increasing the specific capacity.

Pre-potassiation treatment is a crucial step to improve the ICE of carbon materials before assembling PIHCs. There are two methods for this treatment. The first involves direct electrode contact with potassium metal foil or electrochemical pre-potassiation.<sup>[94]</sup> The second method is to immerse the electrode in electrochemically active potassium-arene solutions that contain the radical anions of aromatic hydrocarbons.<sup>[95]</sup> Qian et al. conducted an experiment where they submerged Aglucose-derived carbon (GDC) anode and a commercial AC cathode into a potassium-naphthalene-tetrahydrofuran (K-Nap-

THF) solution. This resulted in an increase in the ICE of the GDC anode from 45.4% to 84.0%, as well as an increase in capacity from 329.8 to 444.8 mAh g<sup>-1</sup> at 0.2 A g<sup>-1</sup>. The cycling CEs were also more stable.<sup>[91]</sup>

### 3.2. MXenes

MXenes is an emerging two-dimensional transition metal (M) carbide and/or nitride (X) material.<sup>[99]</sup> Due to the solid electrical conductivity of MXenes (where  $\text{Ti}_3\text{C}_2\text{T}_x$  has an electrical conductivity of  $\approx 9880 \text{ S cm}^{-1}$  and  $\text{V}_2\text{CT}_x$  has an electrical conductivity of  $3250 \pm 100 \text{ S cm}^{-1}$ ) and strong surface chemistry (coupling with various polar terminations  $-\text{OH}$ ,  $-\text{O}$  and  $-\text{F}$ ), it shows superiority in electrochemistry.<sup>[96,100,101]</sup>

$\text{V}_2\text{C}$ -based MXenes has demonstrated better theoretical capacity than the highly studied mobile ion battery  $\text{Ti}_3\text{C}_2$ . Lian et al. obtained alkaliated  $\text{Ti}_3\text{C}_2$  ( $\text{a}-\text{Ti}_3\text{C}_2$ ) MXenes nanoribbons by treating pristine  $\text{Ti}_3\text{C}_2$  MXenes with continuous oscillation in an aqueous KOH solution.<sup>[102]</sup> The  $\text{a}-\text{Ti}_3\text{C}_2$  anodes exhibited outstanding performance in potassium storage due to their expanded interlayer spacing, narrow-width nanoribbons, and

3D interconnected porous framework. This resulted in improved ion reaction kinetics and better structural stability. At  $20 \text{ mA g}^{-1}$ , the anodes had high reversible capacities of  $136 \text{ mAh g}^{-1}$ , while at  $200 \text{ mA g}^{-1}$ , they had a capacity of  $78 \text{ mAh g}^{-1}$  for PIBs. Ming et al. used  $\text{V}_2\text{C}$ -MXenes as a model system with simple sequential acid/base treatment to boost the storage capacity of  $\text{K}^+$  (Figure 13a). The resulting porous MXenes nanosheets have a strong specific capacity as well as good rate performance, the specific capacity of pristine  $\text{V}_2\text{C}$  was  $98 \text{ mAh g}^{-1}$  at  $50 \text{ mA g}^{-1}$ , while the treated product provided a capacity of  $195 \text{ mAh g}^{-1}$ .<sup>[96]</sup> In addition, they confirmed the charge storage mechanism as a solvent co-intercalation layer by various characterization methods. By coupling the  $\text{K}-\text{V}_2\text{C}$  anode and  $\text{K}_x\text{MnFe}(\text{CN})_6$  cathode, PIHCs were successfully fabricated to achieve a high power density of  $112.6 \text{ W kg}^{-1}$  at an energy density of  $145 \text{ Wh kg}^{-1}$ .

However, the stacking of  $\text{Ti}_3\text{C}_2\text{T}_x$  MXenes nanosheets causes a decrease in their surface area, which leads to a slow potassium ion transport. To solve this problem, a  $\text{Ti}_3\text{C}_2\text{T}_x$  with a 3D structure was constructed by using a spray freeze-drying strategy. The prepared  $\text{Ti}_3\text{C}_2\text{T}_x$  hollow spheres have a large SSA

and a short ion diffusion path.<sup>[98]</sup> It exhibited enhanced capacity and thickness-independent rate performance when used as an anode material, which shows  $122 \text{ mA g}^{-1}$  after 10,000 cycles. In addition, the assembled PIHCs showed a high energy density of  $98.4 \text{ Wh Kg}^{-1}$  and a high power density of  $7015.7 \text{ W Kg}^{-1}$  (Figure 13c). They also used this strategy to prepare other 3D materials such as  $\text{Ti}_3\text{C}_2\text{T}_x$  microtubules, graphene oxide nano-microspheres, etc. This study presents an efficient approach to designing 3D structures using 2D nanosheets, which addresses the issue of stacking in 2D materials during storage and electrode fabrication.

The whole ion intercalation layer is still diffusion-limited due to the limited layer spacing. Therefore, more efforts are still needed to design experimental strategies to increase the layer spacing in MXenes. For example, Zhao et al. constructed 3D  $\text{K}^+$  pre-inserted  $\text{Ti}_3\text{C}_2\text{T}_x$  MXenes with expanded interlayer distance and prepared highly active MXenes-based anode materials by collaborative material design and electrolyte optimization (Figure 13b). The concentrated ether-based electrolyte was optimized to produce a thin SEI on the  $\text{Ti}_3\text{C}_2\text{T}_x$  electrode with pre-inserted  $\text{K}^+$ . It is important for maintaining interfacial stability

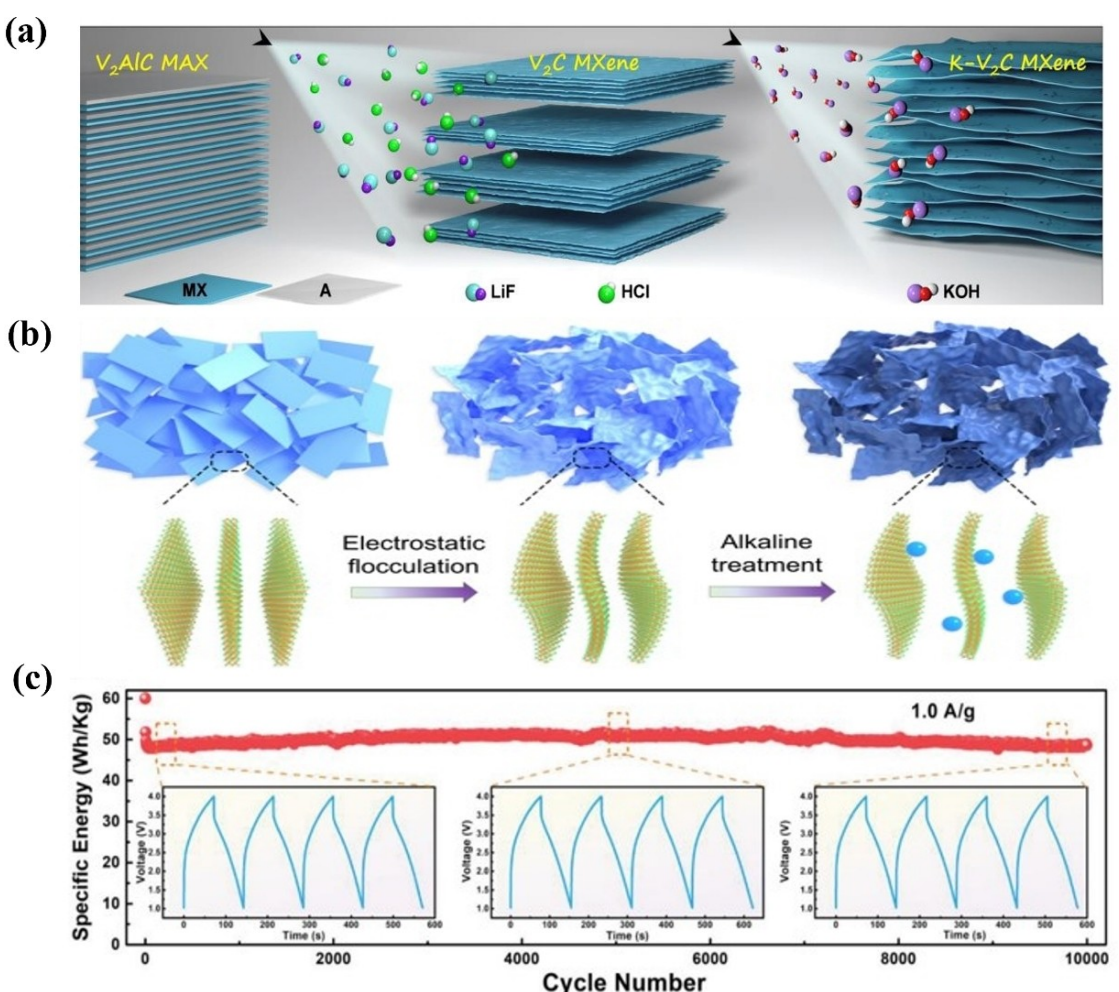


**Figure 13.** a) Schematic illustration of the preparation process of  $\text{K}-\text{V}_2\text{C}$ . Reproduced with permission from Ref. [96]. Copyright (2019) Elsevier. b) Synthesis of 3D  $\text{K}^+$ - $\text{Ti}_3\text{C}_2\text{T}_x$ . Reproduced with permission from Ref. [97]. Copyright (2021) Wiley-VCH. c) Cycling performance of PIHCs (3D- $\text{Ti}_3\text{C}_2$ //HPAC) at  $1.0 \text{ A g}^{-1}$ . Reproduced with permission from Ref. [98]. Copyright (2020) Wiley-VCH.

and reaction kinetics. The 3D  $K^+$ - $Ti_3C_2T_x$  structure, with its porous skeleton and expanded interlayer distance, effectively addresses the issue of large volume expansion during potassium/depotassium. With 3D  $K^+$ - $Ti_3C_2T_x$  as the cathode and AC as the anode, the energy density is  $163 \text{ Wh kg}^{-1}$ , the capacity retention rate is 101%, and the number of cycles reaches 10,000 times.<sup>[97]</sup>

In addition, the flexible MXenes framework can also be used as a fast electron/potassium ion bifunctional conductor for promoting stable potassium storage in graphite electrodes. Cao et al. constructed A graphite nanosheet/MXenes (GNFM) electrode framework by vacuum filtration of a mixed dispersion containing graphite nanosheet (GNF) and MXenes nanosheet materials.<sup>[103]</sup> The continuous MXenes framework constructed 3D channels for fast electron/potassium ion transfer and imparted high structural stability to the GNFM electrode. PIHCs assembled with the anode showed excellent cycling ability and high energy/power density ( $113.1 \text{ Wh kg}^{-1}$  @ $12.2 \text{ kW kg}^{-1}$ ).

### 3.3. Transition metal materials

Transition metals are considered the potential candidates of the anode materials of PIHCs with the advantages of a high specific capacity and high conductivity.<sup>[104]</sup> Alloy reaction is a common mechanism for potassium ion storage in transition metals. During the charge/discharge progress, the potassium ions reversibly move to and from the anode materials to form an alloy via a faradaic reaction.<sup>[20]</sup> Because of the large radius of  $K^+$ , the volume expansion in this process and the slow diffusion kinetics have become the key factors restricting the anode material development of transition metals.<sup>[105]</sup> So, establishing robust microstructures of anode materials legitimately to adapt to the considerable volume expansion and improve the sluggish diffusion kinetics has been given much attention.<sup>[106]</sup> Mainstream design strategies include: 1) choosing pseudocapacitive-dominated materials to boost the electrochemical performance; 2) controlling the size of the anode materials to the nanoscale to improve the kinetic behavior; 3) structuring a remarkable conductive network to shorten the distance of ion diffusion and electron transportation; 4) introducing heteroatom to reform the electronic conductivity and introduce additional active sites.<sup>[107–110]</sup>

#### 3.3.1. Titanium-based materials

Just as lithium titanates play an essential role in lithium-ion hybrid capacitors, potassium titanates (KTO) like  $K_2Ti_6O_{13}$  and  $K_2Ti_2O_5$  are of great potential as transition metal anode materials due to the large spacing for the storage of potassium ions and the low-cost.<sup>[42,112–114]</sup> Bai et al. reported an *in situ* hydrothermal method to synthesize materials (TF-PIMCs) with a stable tunnel structure by combining 1D  $K_2Ti_6O_{13}$  nanobelts with quasi-2D graphite nanosheets (Figure 14a).<sup>[111]</sup> A successful proposal has been made for a multidimensional topotactic host composite anode. This anode utilizes a topotactic potassium-

ion intercalation mechanism, resulting in superior rate performances and cycling stability for both gravimetric and volumetric measurements (Figure 14b). Li et al. synthesized another material in which 1D  $K_2Ti_6O_{13}$  (KTO) nanobelts were interwoven with a 3D porous carbon microstructure (Figure 14c).<sup>[112]</sup> The 3D porous carbon structure facilitates the low specific capacity and sluggish diffusion kinetics of the primitive KTO (Figure 14d). Besides, the hierarchical porosity and 3D structure stop the KTO from agglomeration, which is also conducive to the penetration of potassium-ion in the electrolyte. However, the high SSA of 3D porous carbon structure leads to capacity loss. Zhao et al. prepared carbon-coated  $K_2Ti_2O_5$  microspheres through a spray drying method followed by chemical vapor deposition treatment (Figure 14f).<sup>[113]</sup> After the above synthesis process, the carbon-coated nanorods with an open 3D microstructure (S-KTO@C) were obtained, which was covered by a homogeneous carbon layer with a thickness of 10 nm (Figure 14e). The porous microstructure and the carbon-coated layer guaranteed the fast diffusion kinetics and high electron conductivity. At high current densities, the material exhibited an enhanced intercalation pseudocapacitive behavior (Figure 14g).

In addition, titanium was frequently used in NASICON-type nanospheres such as  $Ba_{0.5}Ti_2(PO_4)_3$  and  $Ca_{0.5}Ti_2(PO_4)_3$ .<sup>[115,116]</sup> NASICON-type structure is flexible in accommodating foreign ions. Meanwhile, the vacancies of potassium ions are replaced by calcium ions. It would facilitate more vacancies at the 3b sites. Dai et al. fabricated  $Ba_{0.5}Ti_2(PO_4)_3$  as an anode and active carbon as a cathode to assemble PIHCs.<sup>[115]</sup> The  $Ba^{2+}$  created vacancies for potassium ions in the crystal structure. Moreover, the morphology of nanospheres ensured that the transportation distance of potassium-ion could be significantly diminished, facilitating the insertion/extraction of  $K^+$ . As desired, the sample showed outstanding cycle performance. Using  $TiO_2$ , the supramolecular assembly-directed one-pot strategy was proposed to form hierarchical nest-like  $TiO_2$ -nitrogen-doped carbon hybrid nanostructures, which showed the considerable potential of  $TiO_2$  used as anode materials for PIHCs.<sup>[117]</sup>

#### 3.3.2. Transition metal compounds

**Transition metal oxides:** Niobium pentoxide ( $Nb_2O_5$ ) was recognized as a potential material for its pseudocapacitive behavior. To weaken the effect of the poor conductivity, Chen et al. reported that the hierarchically porous nanofibers interlace with each other could effectively alleviate the volume expansion to increase the mechanical stability and conductivity consequently.<sup>[118]</sup> Moreover, the material with hierarchically porous structure and N, Se co-doped carbon nanofibers offered a well-developed conductive network (Figure 15a). According to their theoretical calculation, high-concentration KFSI took a shortcut to form a highly robust SEI film and showed a better thermodynamic reactivity. Luo et al. tried to find an efficient growth route for the  $CoFe_2O_4$ , which has a robust porous structure with a high SSA and abundant mesopores (Figure 15b).<sup>[119]</sup> Besides, introducing carbon nanotubes into the hybrid aerogel significantly enhances the relation between the

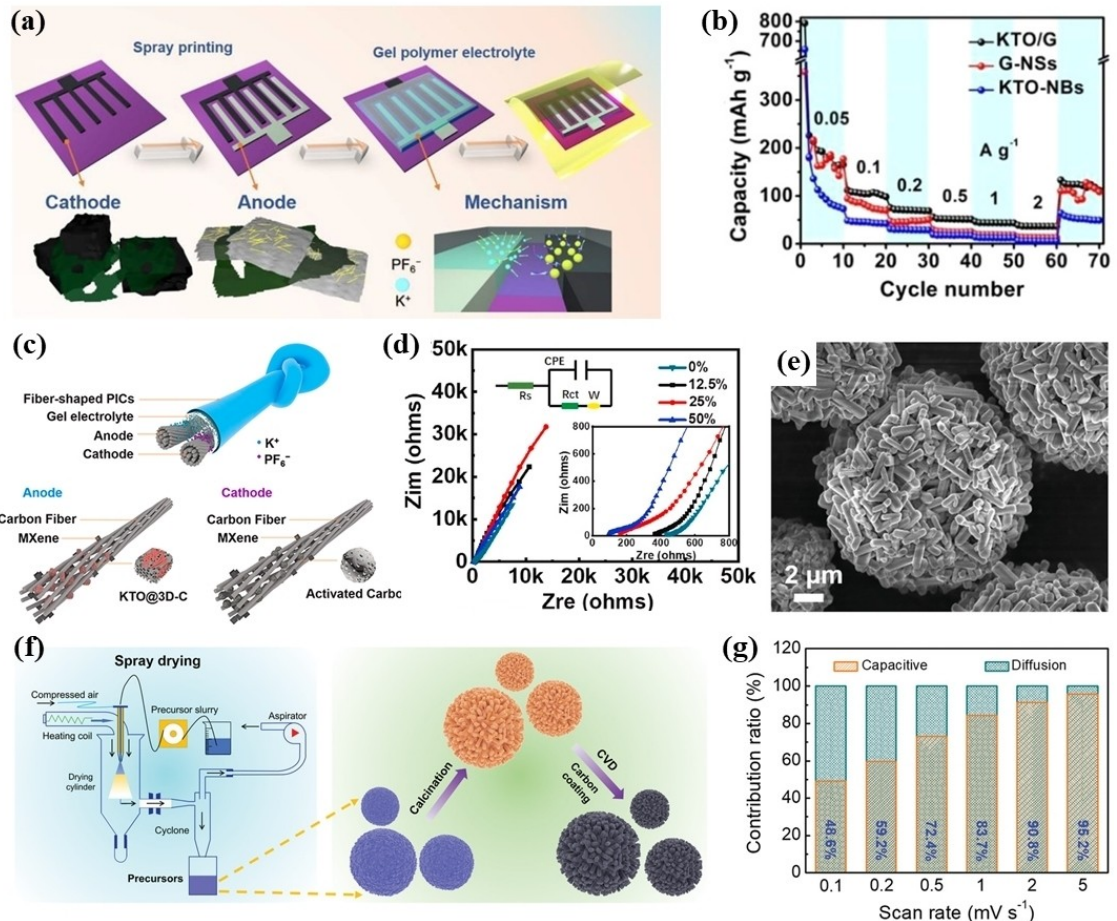


**Figure 14.** a) Fabrication procedures, electrodes, and energy storage mechanism of TF-PIMCs. b) Gravimetric rate performances of the KTO/graphite anode. Reproduced with permission from Ref. [111]. Copyright (2021) American Chemical Society. c) Schematic illustration of the fiber-shaped PIHCs. d) Nyquist plots of fiber-shaped PIHCs with various MXenes additions. Reproduced with permission from Ref. [112]. Copyright (2022) Elsevier. e) SEM image of S-KTO@C. f) Schematic illustration of the preparation process for S-KTO@C. g) The capacitive contribution histograms of the S-KTO@C electrodes at different scan rates. Reproduced with permission from Ref. [113]. Copyright (2020) Wiley-VCH.

nanowires and nanoparticles. It is common knowledge that carbon nanotubes possess high electronic conductivity. Thus, introducing carbon nanotubes could remarkably improve the conductivity of composite materials, enhance the rate performance and become the substrate of  $\text{CoFe}_2\text{O}_4$ .  $\text{CoFe}_2\text{O}_4$ /carbon nanotubes composites exhibited a reversible capacity of  $180 \text{ mAh g}^{-1}$  at  $100 \text{ mA g}^{-1}$  with no capacity loss after 200 cycles (Figure 15c). Chang et al. have successfully synthesized a nanonetwork of bismuth antimonate ( $\text{BiSbO}_4$ ) using cetyltrimethylammonium bromide-mediated growth. The nanonetwork has an architecture of perpendicularly crossed single crystal nanorods, which predominantly expose  $(001)$  planes (Figure 15d and e).<sup>[120]</sup>

**Transition metal phosphides:** Transition metal phosphide-based materials delivered high theoretical capacities, making them excellent transition metal anode materials of PIHCs. Wang et al. demonstrated that sub-4 nm  $\text{Co}_2\text{P}$  nanorods attached to reduced graphene oxide ( $\text{Co}_2\text{P}@r\text{GO}$ ) could afford the request for high electrochemical performance (Figure 16a and b).<sup>[121]</sup> To reduce the volume expansion during the charging/discharging process, combining the ultrafine  $\text{Co}_2\text{P}$  with rGO offered a huge

carbon network of conductivity, which can improve the conductance of the anode materials. The experiments showed that the ultrafine nanostructure had three advantages: i) Stabilizing the electrode structure to ensure integrity. ii) Reducing the solid-state diffusion length of potassium ions. iii) Providing more electrochemical reaction sites. Zong et al. synthesized MoP@NC, a series of MoP nanoparticle splotched nitrogen-doped carbon nanosheets (Figure 16c).<sup>[122]</sup> The study found that smaller MoP nanoparticles achieved a larger three-phase boundary, which favored competitive binding energy toward potassium ions. The use of a water-soluble polyacrylamide hydrogel helped reduce the volume expansion of the MoP nanorods during the charging/discharging process. Moreover, it offered a conductive path for potassium ions to diffuse and electrons to transfer. The ultrafine MoP nanoparticles could activate the neighboring areas in nitrogen-doped carbon nanosheets skeletons and generate partial MoP ionic bonds. Thus, the binding energy to potassium ion could be efficiently improved and the conductivity was demonstrated to be enhanced (Figure 16d).

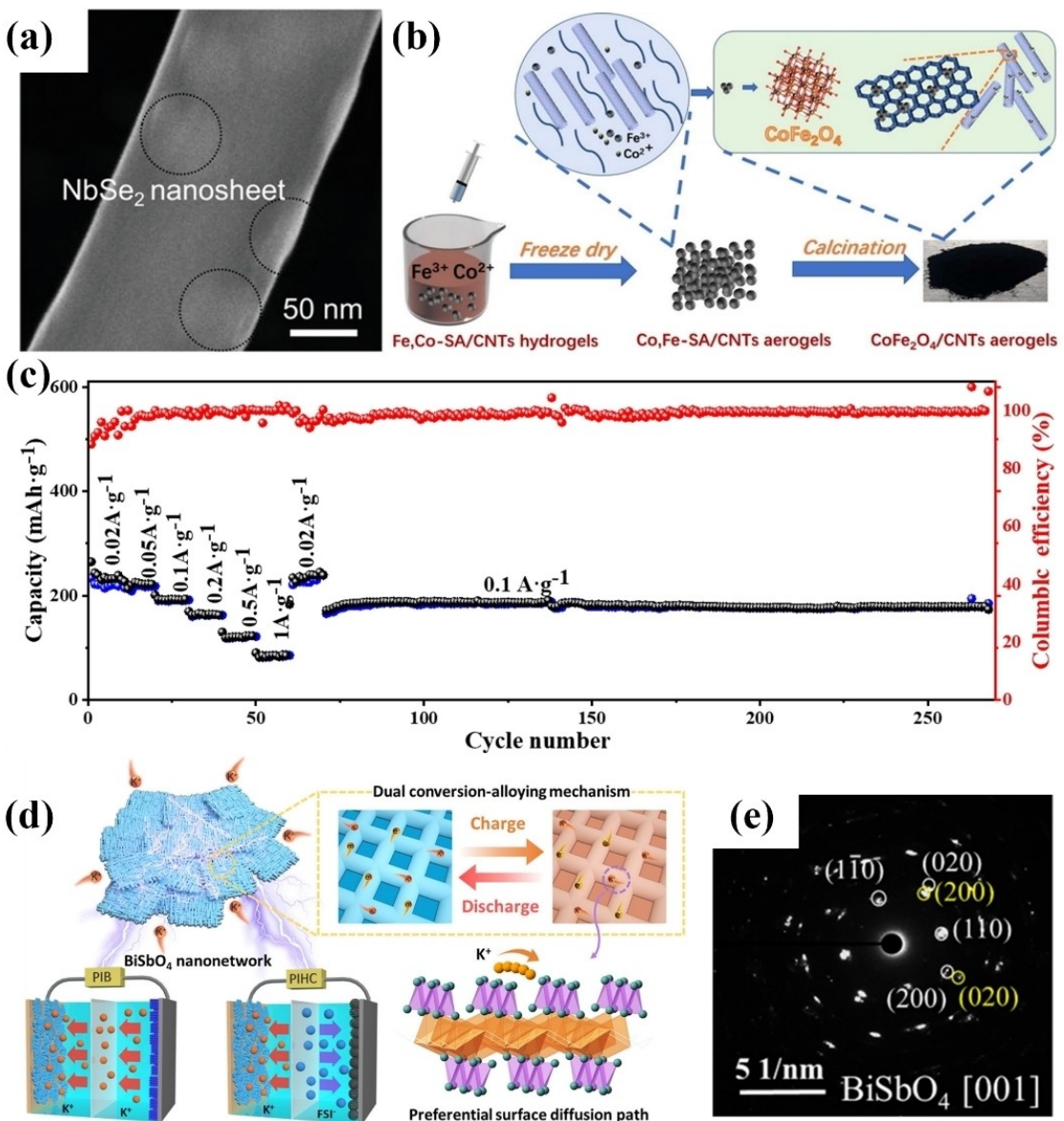


**Figure 15.** a) SEM image of  $\text{NbSe}_2/\text{NSeCNFs}$  composite. Reproduced with permission from Ref. [118]. Copyright (2020) Wiley-VCH. b) The schematic diagram of  $\text{CoFe}_2\text{O}_4$  and CNTs composites. c) Rate and cycling performances of the  $\text{CoFe}_2\text{O}_4$  electrode. Reproduced with permission from Ref. [119]. Copyright (2021) Academic Press Inc. d)  $\text{BiSbO}_4$  nanonetwork electrode and its working mechanism for  $\text{K}^+$  Storage and applications on PIBs and PIHCs. e) (001)-orientated plane of a  $\text{BiSbO}_4$  network. Reproduced with permission from Ref. [120]. Copyright (2022) American Chemical Society.

**Transition metal selenides:** Transition metal selenides allow metal atoms to insert/extract between two layers of chalcogenides with layered structures. Nitrogen-doped  $\text{MoSe}_2/\text{G}$  was synthesized with favorable pseudocapacitive potassium storage.<sup>[123]</sup> The diatomite was selected as the precursor. Its hierarchically versatile morphology provided open frameworks and ample porosities to enhance potassium ion diffusion and electron transportation (Figure 16e). Besides, the unique 3D biomorphic nanoarchitecture offers abundant active sites resulting in significant pseudocapacitive behavior (Figure 16f).

**Transition metal carbides:** As special interstitial alloys, Transition metal carbides play a role in high conductivity and mechanical and chemical stability. Min et al. utilized a simple

electrospinning method to create a flexible and self-supporting anode for PIBs using  $\text{Mo}_2\text{C}/\text{NCNFs}$ .<sup>[124]</sup> The anode consists of  $\text{Mo}_2\text{C}$  quantum dots embedded in N-doped carbon nanofibers, which also serve as conductive pathways for potassium ions and electrons. Additionally, the use of N-doped carbon nanofibers eliminates the need for conductive agents and adhesives. What is more, manganese is also a significant element in synthesizing superior anode materials, such as  $\text{MnO}_2$ ,<sup>[125]</sup>  $\text{K}_x\text{MnO}_2$ ,<sup>[126]</sup> and  $\text{K}_{0.45}\text{Mn}_{0.5}\text{Co}_{0.5}\text{O}_2$ .<sup>[127]</sup>

**Other transition metal compounds:** The study of transition metal compounds is immature, and many metal-based materials are being investigated. Lang et al. investigated an Sn-based anode material with a high surface area and mesoporous structure.<sup>[128]</sup> The typical galvanostatic charge/discharge curves

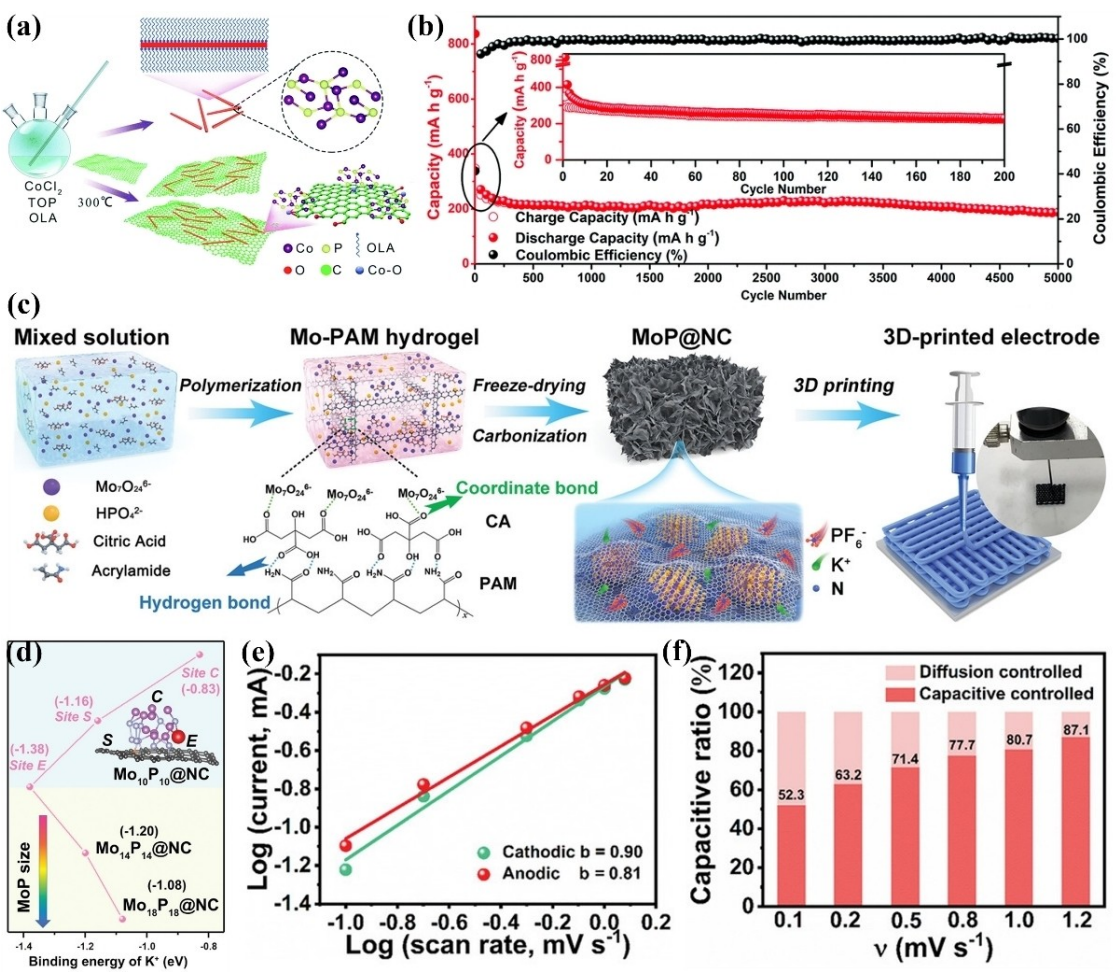


**Figure 16.** a) Schematic illustration of the fabrication of the ultrafine Co<sub>2</sub>P NRs and U-Co<sub>2</sub>P@rGO-14 nanocomposite. b) Long-term cycling of U-Co<sub>2</sub>P@rGO-14 at a current density of 200 mA g<sup>-1</sup>. Reproduced with permission from Ref. [121]. Copyright (2019) Royal Society of Chemistry. c) Schematic illustration for the MoP@NC composites and 3D-printed electrode synthetic procedure. d) Calculated K<sup>+</sup> (red atom) binding energy values on different sites of Mo<sub>10</sub>P<sub>10</sub>@NC, as well as the rims of Mo<sub>14</sub>P<sub>14</sub>@NC and Mo<sub>18</sub>P<sub>18</sub>@NC. The inset is the constructed model for K<sup>+</sup> binding on the different sites of Mo<sub>10</sub>P<sub>10</sub>@NC, where the indices C, E, and S represent the sites of the center of MoP, a rim of MoP and NC, and the surface of exposed NC, respectively. Reproduced with permission from Ref. [122]. Copyright (2021) Wiley-VCH. e) Plot of log (peak current) versus log (scan rate) of cathodic/anodic peaks from CV scans and b-value determination lines of N-MoSe<sub>2</sub>/G electrode. f) Pseudocapacitive contribution ratio at different scan rates of N-MoSe<sub>2</sub>/G electrode. Reproduced with permission from Ref. [123]. Copyright (2020) Wiley-VCH.

of the PIHCs using the as-prepared material as anode material exhibited a combination of the alloying/dealloying and adsorption/desorption mechanisms. In the process of alloying/dealloying, the K<sub>2</sub>Sn alloy exhibited favorable electronic conductivity, as evidenced by the density of states analysis, which facilitated rapid electron transport. Notably, A gel polymer electrolyte modified with PVDF-HFP and soaked in 1 M KPF<sub>6</sub> (EC-DMC-EMC 4:3:2 v/v/v) was chosen as both the electrolyte and separator for the PIHCs. The experiment showed that the as-made gel polymer electrolyte with 5 wt% Poly (ethylene oxide) has a 3D porous structure and high ionic conductivity. Compared to the liquid electrolyte, the gel polymer electrolyte could be part of an artificial solid electrolyte interphase film to provide long-term and stable structural protection for the anode and protect the alloying/dealloying process equally. Therefore, the capacity of PIHCs is exceptionally stable for over 2000 cycles at 3.0 Ag<sup>-1</sup> with a CE that is close to 100%.

Currently, binary alloys<sup>[129]</sup> and even ternary alloys<sup>[130]</sup> gradually show excellent application potential.

## 4. Cathode Materials for PIHCs

### 4.1. Carbon-based materials

The ideal cathode materials play an indispensable role in PIHCs. The most commonly used cathode materials are carbon materials with high SSA, which can accelerate electrolyte penetration and ion transfer.<sup>[133,134]</sup> Among these carbon materials, AC plays a dominant role, which comes from various sources, and the structure can be adjusted.

Commercial AC is the most commonly used AC in current research.<sup>[129,136]</sup> The commercial AC cathode displays impressive charge and discharge specific capacity of 108.3 mAhg<sup>-1</sup> and

86.5 mAh g<sup>-1</sup>, respectively, at 0.1 A g<sup>-1</sup> (the first cycle) (Figure 17a).<sup>[73]</sup> The charge-discharge curves are symmetric without a major voltage platform, indicating typical capacitive behavior. Additionally, the commercial AC cathode demonstrates excellent rate performance (Figure 17b). Qian et al. suggested a chemical pre-potassiation approach to enhance the CE of commercial AC electrodes.<sup>[91]</sup> They found that the pre-potassiated electrode (CAC-CP) could prompt the electrolyte to form a uniform and dense KF-rich CEI film, which effectively curbs the oxidation decomposition of the electrolyte at 4.2 V and even up to 4.5 V. The CAC-CP electrode shows a capacity of 104.2 mAh g<sup>-1</sup> with a capacity retention ratio of 75.7% (at 1.0 A g<sup>-1</sup> after 1000 cycles), while the commercial AC electrode only exhibits a capacity of 89.2 mAh g<sup>-1</sup> with the capacity retention ratio of 29.9%.

Biomass-derived AC is widely used because of its comprehensive source and low cost. The composition of plant cell walls varies, resulting in unique carbon structures in different biomass residues. Pine needle-activated carbon (PNAC) was created through a one-step carbonization/activation process. Analysis of PNAC showed the presence of mainly C and O elements. Orange-peel-derived activated carbons (OPAC) were fabricated by the carbonization/activation process.<sup>[131]</sup> The structure of OPAC is characterized by a 3D open-porous architecture made

up of thin nanosheets. This unique structure has the advantage of improving electron transport while maintaining good ionic conductivity. The TEM image (Figure 17c) shows that the nanosheets are thin and transparent, while the HRTEM image (Figure 17d and e) indicates the presence of Agraphitic diffusion layer.

KOH activation is an effective method in the preparation of carbon materials with high SSA, such as corn stalk-derived porous carbons,<sup>[137]</sup> pear wood charcoal derived AC,<sup>[138]</sup> activated B, N stabilization effect on porous hollow multi-cavity carbon spheres,<sup>[139]</sup> polyaniline derived porous carbon,<sup>[140,141]</sup> activated carbon nanofibers,<sup>[142]</sup> and so on.<sup>[135,143,144]</sup> Yang et al. converted ethylene diamine tetraacetic acid tetrasodium (EDTA-4Na) to a 3D nitrogen-doped framework carbon (3DNFC) through simple calcination.<sup>[74]</sup> The 3DNFC can be converted into a 3D nitrogen-doped framework-activated carbon (3DNFAC) with a high SSA of 3839 m<sup>2</sup> g<sup>-1</sup> and good capacitance performance when KOH activation is utilized. The 3D network structure of the 3DNFC is well preserved, and the carbon sheets contain numerous uniformly distributed mesopores, as depicted in Figure 17(f). When using 3DNFC as anode and 3DNFAC as cathode, the PIHCs exhibit excellent cycling stability (91.7% after 10 000 cycles at 2.0 A g<sup>-1</sup>).

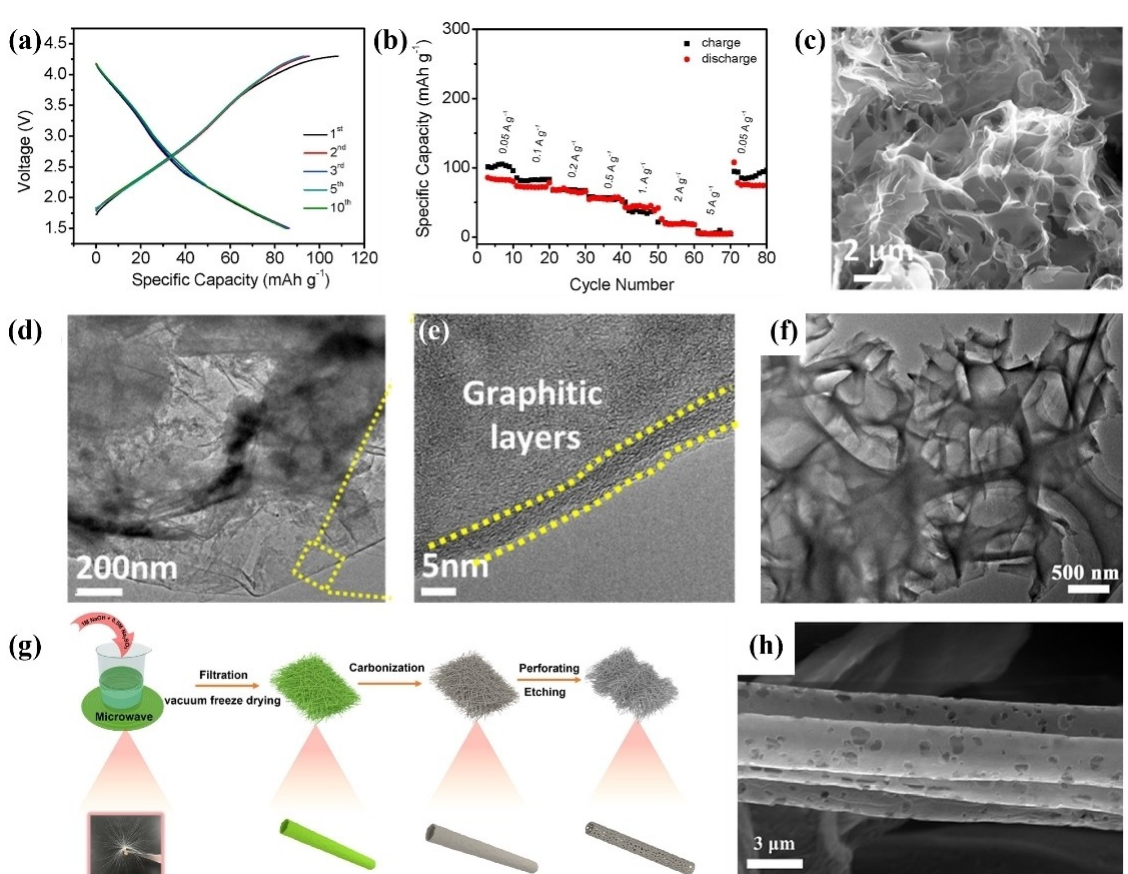


**Figure 17.** a) GCD curves of CAC at 0.1 A g<sup>-1</sup>. b) Rate capability of CAC cathode. Reproduced with permission from Ref. [73]. Copyright (2020) Elsevier. c) SEM and d, e) HRTEM images of OPAC. Reproduced with permission from Ref. [131]. Copyright (2021) Elsevier. f) TEM image of 3DNFAC. Reproduced with permission from Ref. [74]. Copyright (2019) Elsevier. g) Graphic illustration of synthesizing FSF-PCTs. h) SEM image of FSF-PCTs. Reproduced with permission from Ref. [132]. Copyright (2021) American Chemical Society.

In addition, there are other ways to prepare porous AC. A versatile freestanding electrode made up of porous carbon tubes (FSF-PCTs) was created by Wang et al. using a combination of microwave treatment of fluffs through a mixture of 1 M NaOH and 0.5 M Na<sub>2</sub>SO<sub>3</sub>, carbonization, and CO<sub>2</sub> perforation.<sup>[132]</sup> The resulting FSF-PCTs exhibit a 3D interconnected network structure composed of porous carbon tubes, each with a thickness of approximately 200 μm and perforated holes, as shown in Figure 17(g and h). Thanks to these characteristics, FSF-PCTs show exciting performance in both anode and cathode. Furthermore, symmetric PIHCs based on FSF-PCTs were successfully developed without the use of current collectors, binders, or conductive agents. This achievement not only simplifies the production process but also reduces costs significantly.

#### 4.2. Prussian blue and its analogues

Prussian blue is a mixed-valence ferricyanide complex with a repeating unit of potassium ferricyanide or sodium ferricyanide hexahydrate. The field of study has been extended since its discovery in the early 18th century. From Prussian blue itself to its derivatives (with the general formula C<sub>n</sub>A<sub>p</sub>[B(CN)<sub>q</sub>]<sub>-aq</sub>, where A and B are transition metals in different oxidation states. C is an alkali metal and may also be absent). Due to its four interconnected cyanide ≡ ligands, it forms an open framework of large gap sites for potassium ions, which facilitate the regulation of different alkali ions, enables rapid embedding and de-embedding of large-sized potassium ions with good electro-

chemical reversibility and high stability, and thus have great promise for applications in PIHCs, etc.<sup>[147–149]</sup>

Prussian blue has the advantages of low cost and easy synthesis. The successful application of Prussian blue in PIHCs will be conducive to large-scale fixed energy storage. Zhou et al. synthesized electrode materials that provide a new approach to prepare high-performance electrode materials.<sup>[145]</sup> Aqueous PIHCs based on activated carbon and high-quality cubic Prussian blue were successfully prepared in a 0.5 mol L<sup>-1</sup> K<sub>2</sub>SO<sub>4</sub> electrolyte solution by a simple one-step synthesis of cubic Prussian blue crystals. It shows excellent electrochemical behavior in aqueous K<sub>2</sub>SO<sub>4</sub> solutions (Figure 18a and b). The prepared ionic capacitors exhibited a maximum energy density of 28 Wh kg<sup>-1</sup> at a current density of 1 Ag<sup>-1</sup> and excellent cycling stability at a current density of 2 Ag<sup>-1</sup>, with a capacity retention rate of nearly 98% over 1200 cycles. Furthermore, Xue et al. proposed a cyanoperoxide K<sub>x</sub>MnFe(CN)<sub>6</sub> (0 ≤ x ≤ 2) as a cathode material.<sup>[150]</sup> As a Prussian analogue, the cyanotungstenite framework MnFe(CN)<sub>6</sub> can reversibly accept nearly two K<sup>+</sup> in each chemical formula unit, which means it can be a rechargeable potassium cathode host and has a theoretical capacity of up to 156 mAh g<sup>-1</sup>. Ming et al. fabricated full cells by coupling a K-V<sub>2</sub>C anode and a Prussian blue analogue (K<sub>x</sub>MnFe(CN)<sub>6</sub>) cathode, which can be used over a wide voltage range of 0.01–4.6 V over a wide voltage range and have an average operating voltage of up to 3.3 V (Figure 18c).<sup>[96]</sup> In addition, the PIHCs (K-V<sub>2</sub>C//K<sub>x</sub>MnFe(CN)<sub>6</sub>) can obtain a high capacity of 145 mAh g<sup>-1</sup> at 100 mAh g<sup>-1</sup> and achieve a high energy density of 145 Wh kg<sup>-1</sup> at a power density of 112.6 W kg<sup>-1</sup>. To further improve the energy storage of PIHCs,

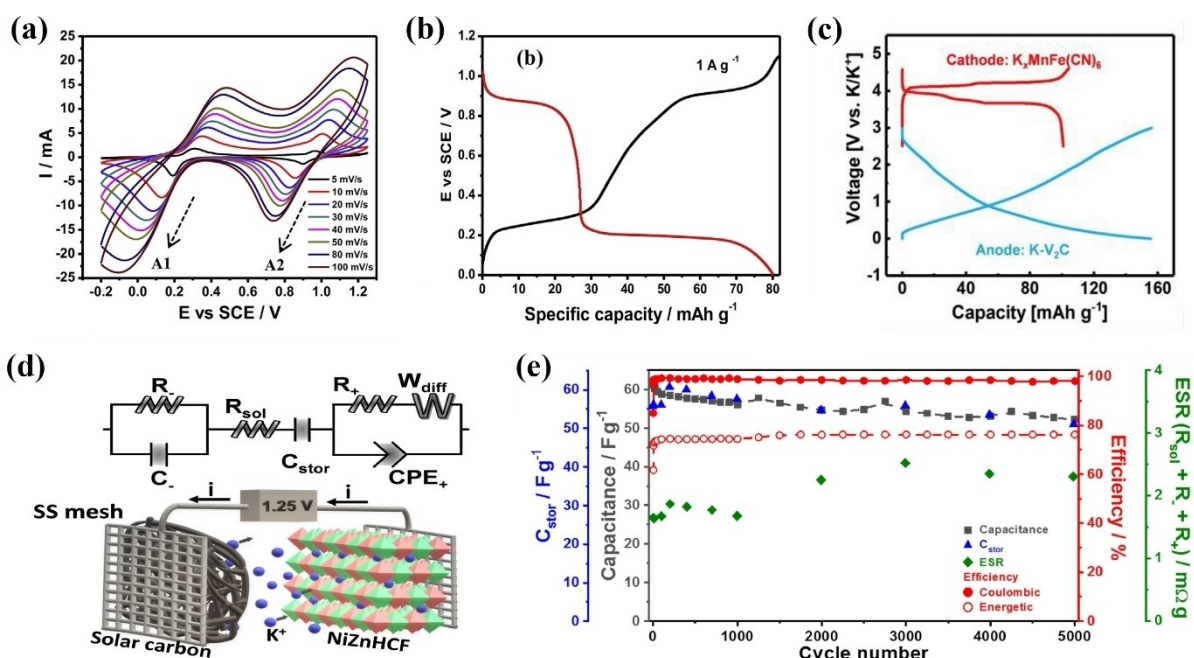


**Figure 18.** a) CV curves at different scan rates from 5 to 100 mV s<sup>-1</sup> and b) GCD curves at 0.5 Ag<sup>-1</sup> of the PB electrode. Reproduced with permission from Ref. [145]. Copyright (2017) Elsevier. c) GCD curves of K-V<sub>2</sub>C and K<sub>x</sub>MnFe(CN)<sub>6</sub>. Reproduced with permission from Ref. [96]. Copyright (2019) Elsevier. d) Electric equivalent circuit employed to fit the experimental EIS. e) Impact of the number of cycles (@ 2.5 Ag<sup>-1</sup>) over the capacitance measured from GCD and EIS, the Coulombic and energy efficiency, and the ESR derived from EIS ( $\text{ESR} = R_{\text{sol}} + R_+ + R_{\text{stor}}$ ) of the PIHCs (solar carbon//Zn-NiHCF). Reproduced with permission from Ref. [146]. Copyright (2020) Elsevier.

Diego et al. prepared hybrid hexacyano high-iron Ni–Zn by simple chemical precipitation, exploiting the synergy between zinc and nickel atoms, providing high reversibility, high potential and stability (Figure 18d).<sup>[146]</sup> The assembled PIHCs maintain an initial capacitance of 85% at  $2.5 \text{ A g}^{-1}$  after 5000 cycles, with a CE close to 100% (Figure 18e). The practical application potential of Prussian blue and its analogues in the production of PIHCs is further proved.

### 4.3. Transition metal materials

Transition metal materials are gaining attention due to their high capacity and unique properties, as they are able to meet the increasing demand for high capacity and fast rate performance. Inactive metal atoms present in transition metal oxides are converted into metal phases through conversion reactions, which enhances their electronic conductivity and performance multiplier capabilities.<sup>[151]</sup> Because of its high energy density and two-dimensional open frame, the layered transition metal oxide materials can facilitate the rapid migration of potassium ions, which makes it a feasible cathode candidate for PIHCs.<sup>[152]</sup> Hari Vignesh Ramasamya et al. synthesized P3-K<sub>0.45</sub>Mn<sub>0.5</sub>Co<sub>0.5</sub>O<sub>2</sub> nanosheets by a simple sol-gel method for novel non-aqueous PIHCs with P3-K<sub>0.45</sub>Mn<sub>0.5</sub>Co<sub>0.5</sub>O<sub>2</sub> as cathode and commercial AC anode. It was obtained that the presence of binary (Mn–Co) transition metals in the structure suppressed K<sup>+</sup>/vacancy ordering, resulting in smooth charge/discharge curves and excellent stability in cycling. The stability of up to 30,000 cycles can also be achieved at  $10 \text{ A g}^{-1}$ . The excellent electrochemical performance demonstrates the potential of transition metal compounds as future PIHCs applications.<sup>[153]</sup>

P.S. The unit of energy density is Wh kg<sup>-1</sup>, and the unit of power density is W kg<sup>-1</sup>.

## 5. Conclusions and Perspective

In conclusion, due to abundant potassium resources, low standard electrode potential, low cost, high energy density, and high power density, PIHCs have received a lot of research and attention in recent years (Table 1). Some encouraging results have been achieved in this field up to now, especially in the development of anode and cathode materials. However, due to the thermodynamic instability, kinetic hysteresis, and the dynamic mismatch between anode and cathode materials, the electrochemical properties and processes of PIHCs are also complicated, which have a comprehensive impact on the overall performance of PIHCs systems. Therefore, many research works related to material development have been dedicated to overcoming the drawbacks. This review expounds on recent advances in PIHCs, including energy storage mechanisms, existing issues, hybrid capacitor design, and cycle stability. Significantly, the research progress and achievements of anode and cathode materials in recent years are reviewed in detail. The electrode materials are classified into carbon-based materi-

als, MXenes, transition metal materials, and Prussian blue and its analogues.

Although there have been some advances, the current research on PIHCs is not mature enough. To make breakthroughs in electrode materials, electrolytes, membranes, and so on, further efforts from researchers are needed. The challenge and perspective for PIHCs can be summarized as follows:

- 1) The design of anode materials is exceptionally significant in preparing PIHCs with high energy density, high power density, and good cycling performance. Carbon-based materials are the most widely used materials, with characteristics of low cost. Hard carbon has been widely investigated among these materials due to its suitable layer spacing but has low ICE and slow reaction kinetics. Therefore, porous materials can be designed to shorten the diffusion path of ions. To solve the problem of low ICE, it can be improved by pre-potassiation, which is a crucial technology to avoid electrolyte consumption and compensate for the initial potassium loss, thereby ensuring its high stability in subsequent cycles. MXenes have high electrical conductivity, defined layered structure, and rich surface chemistry. However, current synthesizing methods of MXenes usually involve using hydrofluoric acid. Therefore, it is significant to explore environmentally friendly etching agents and develop low-cost etching processes. Transition metal materials have been widely studied because of their high theoretical capacity and large reserves. However, their poor conductivity and structures are easy to destroy. Therefore, good structural design can be used to reduce the influence of ion embedding and ejection on structure and volume. In addition, it can be combined with carbon modification or doping strategies to improve the conductivity of the materials.
- 2) Developing a high-capacity cathode is the top priority. The most commonly used cathode materials are activated carbons with high SSA, porous structure, low cost, and mature fabrication technology. Typically, activated carbons are prepared from carbon-rich materials through an activation with KOH at high temperatures, but activated carbons have a lower specific capacity than anode materials. Therefore, improving the adsorbability of activated carbons is a problem that needs to be solved. Possible strategies include heteroatom doping, template method, pre-potassiation, using the same anode material, or exploring new materials with specific structures.
- 3) In the whole device of PIHCs, the dynamics of anodes and cathodes do not match because of the different rates of Faraday reaction on the surface of the anodes and cathodes. Therefore, it is necessary to increase the power of anodes and the capacity of cathodes, as well as carefully calculate and match the mass of the electrode material so that the anodes and cathodes are thermodynamically and dynamically matched.
- 4) To realize the practical value of PIHCs, the performance of the other components is also critical, including electrolytes<sup>[154]</sup>, diaphragms, current collectors (including Cu,

**Table 1.** Summary of PIHCs described in detail in the article.

PIHCs (anode//cathode)	Max energy density @Power density	Energy density @Max power density	Cycle number	Retention	Voltage [V]	Electrolytes	Ref.
graphite//AC	12@22	11@1500	55000	97 %	0.5–3.5	1 M KPF <sub>e</sub> /EC-DEC	[31]
EGOC//AC	114@373	53@12920	2500	89 %	0.01–4	0.8 M KPF <sub>e</sub> /EC-DEC	[33]
LAP-rGO-CDs//AC	119@536	89@5352	1000	~ 100 %	1–4	0.8 M KPF <sub>e</sub> /DC-DEC	[35]
OAC/G//PNAC	157@500	42@14965	5000	75 %	0–5	0.8 M KPF <sub>e</sub> /DC-DEC	[37]
CoV <sub>2</sub> O <sub>6</sub> @GO//AC	151@113	78@22500	3000	96.8 %	0.5–4	0.8 M KPF <sub>e</sub> /DC-DEC	[38]
NPG//AC	104@761	42@14976	1000	65 %	1–4	1 M KPF <sub>e</sub> /EC-DEC	[40]
CBC@G//ACBC	172@172	44@22000	5000	81.5 %	0.01–4	0.8 M KPF <sub>e</sub> /EC-DEC	[41]
ALD KTO//AC	119@118	35@4700	4000	70 %	0.5–4.3	0.8 M KPF <sub>e</sub> /EC-DEC	[42]
SCNs//ACNs	124@199	59@8188	9000	89.4 %	0.01–4	–	[43]
PCNF//aPCNF	110@200	45@10000	10000	83.5 %	0.01–4	0.8 M KPF <sub>e</sub> /EC-DMC	[44]
N-GQD@ASC-500//PC	171@100	50@20000	3000	84.2 %	0.01–4	1 M KPF <sub>e</sub> /EC-DMC	[45]
HC//AC	75@184	26@6044	–	–	0.01–4.2	0.8 M KPF <sub>e</sub> /EC-DEC	[46]
CFMS//CFMS	58@1158	39@7800	10000	90 %	0.01–3.8	0.8 M KPF <sub>e</sub>	[47]
PNTCDA@900//AC	36@162	20@600	800	71.2 %	0.01–3.5	0.8 M KPF <sub>e</sub> /EC-DEC	[48]
WPCS//WPCS	108@280	44@15400	4000	87 %	0–4.5	1 M KPF <sub>e</sub> /EC-DMC	[49]
KPCR//AC	157@14000	~ 3@ ~ 160000	10000	99.6 %	0–2.5	30 M CH <sub>3</sub> COOK	[50]
BPCS//NPC	103@15000	–	5000	90 %	0–4.5	–	[51]
BCCFs-800//AC	119@186	52@2187	1000	~ 100 %	0.5–4	1 M KPF <sub>e</sub> /EC-DMC-EMC	[52]
BCNBs//NSPC	178@1000	55@20000	2000	70.6 %	0–4	1 M KFSI/EC-DEC	[65]
AC//AC	51@1260	15@20110	10000	~ 80 %	0.01–3	0.8 M KPF <sub>e</sub> /EC-DEC	[54]
SEG//SEG	51@600	25@9600	10000	80 %	0.01–3	0.8 M KPF <sub>e</sub> /EC-DEC	[55]
OCMS//3DPC	141@644	65@6347	8500	~ 60 %	0.5–3.7	0.8 M KPF <sub>e</sub> /EC-PC	[56]
HCMB//AC	152@350	112@17500	1000	90 %	2.5–4.5	0.8 M KPF <sub>e</sub> /EC-DMC	[57]
N-CHC//AC	127@203	20@2371	600	~ 84 %	0.5–4	1 M KPF <sub>e</sub> /EC-DEC	[58]
FOCN//NPC	193@494	20@22324	2000	99.3 %	0–4	KFSI/DME-HFE	[59]
S-C <sub>com</sub> //S-PC <sub>DS-outer</sub>	151@200	30@10000	1000	~ 75 %	0–4	0.8 M KPF <sub>e</sub> /EC-DMC	[60]
MDPC//PDPC	120@260	22@26000	120000	79 %	1–4.2	0.8 M KPF <sub>e</sub> /EC-DMC-EMC-FEC	[63]
TiO <sub>2</sub> /C@NPSC//ZDPC	114@210	37@21000	10000	91.6 %	0–4.2	0.8 M KPF <sub>e</sub> /EC-DEC	[64]
NHCS//ANHCS	114@101	19@8203	5000	80.4 %	0.01–4	0.8 M KPF <sub>e</sub> /EC-DEC	[66]
NHCNs//BDPC	155@210	70@10500	1300	81.1 %	0.01–4.2	0.8 M KPF <sub>e</sub> /EC-DEC	[72]
NCP//AC	90@ ~ 250	~ 20@3000	5000	80.4 %	1.5–4.3	1 M KPF <sub>e</sub> /EC-DEC-DMC	[73]
3DNFC//3DNFAC	164@210	76@21000	10000	91.7 %	1.5–4.2	0.8 M KPF <sub>e</sub> /EC-DMC	[74]
NPC//AC	177@967	84@19348	3000	81.6 %	0.01–4	0.8 M KPF <sub>e</sub> /EC-DEC	[75]
PN-PanC//PN-PanC	156@71	22@11,309	20000	93.4 %	0.1–3.8	1 M KFSI/EC-DEC	[80]
NPMC//PNAC	82@460	~ 35@ ~ 10500	1000	90 %	0–4.5	0.8 M KPF <sub>e</sub> /EC-DEC	[81]
PNHCS//AC	179@198	31@5277	3000	80.8 %	0.01–3	1 M KFSI/EMC	[82]
S-N-PCN//AC	187@99	76@5136	3000	86.4 %	0.01–3	0.8 M KPF <sub>e</sub> /EC-DEC	[86]
N, S-3DHPC-600//AC-800	131@210	56@16800	5000	86.8 %	0.01–4.2	0.8 M KPF <sub>e</sub> /EC-DEC	[87]
NOCS//AC	167@1001	113@17000	2000	~ 67 %	0.01–4.1	3 M KFSI/EC-DEC	[88]
PCSS//AC	~ 65@ ~ 70	33@8525	8000	~ 100 %	0.01–4	3 M KFSI/DME	[92]
P/O-PCS//AC	158@223	11@1380	30000	94.5 %	0.01–4	1 M KFSI/EC-DEC	[89]
MHC//ACF	181@70	62@4000	5000	89 %	0–4	1 M KPF <sub>e</sub> /EC-DMC	[90]
GDC-CP//CAC-CP	173@594	124@15437	10000	~ 85 %	–	0.8 M KPF <sub>e</sub> /EC-PC	[91]
K-V <sub>2</sub> C//K <sub>x</sub> MnFe(CN) <sub>6</sub>	145@113	31@3026	200	95 %	0.01–4.6	0.8 M KPF <sub>e</sub> /EC-DEC	[96]
3D-Ti <sub>3</sub> C <sub>2</sub> /HPAC	98@121	19@7016	10000	100 %	1–4	0.8 M KPF <sub>e</sub> /EC-DEC	[98]
3D K <sup>+</sup> -Ti <sub>3</sub> C <sub>2</sub> X//AC	163@ ~ 130	12@8700	10000	101 %	0.01–4	4 M KFSI/DEC	[97]
GNFM//AC	113@49	62@12200	600	74.1 %	2–4.2	2 M KFSI/TEP	[103]
S-KTO@C//AC	57@ ~ 150	~ 10@1740	3000	80.3 %	0.01–3.5	1 M KFSI/EC-DEC	[113]
BTP/C NSs//AC	566@129	24@4577	2000	~ 80 %	1–3.8	1 M KFSI/EC-DEC	[115]
TiO <sub>2</sub> /NC-HN//AC	109@98	~ 30@ ~ 5000	30000	–	0.01–3.8	0.8 M KFSI/EC-DMC	[117]
NbSe <sub>2</sub> /NSeCNFs//AC	133@180	18@4000	10000	83 %	0.01–3.8	5 M KFSI/EC-DMC	[118]
BiSbO <sub>4</sub> //AC	118@101	23@3932	4000	67 %	0–3.9	1 M KFSI/DMC	[120]
U-Co <sub>2</sub> P@rGO-14//AC	87@12	10@4265	1000	68 %	1–4	1 M KPF <sub>e</sub> /EC-DEC-EMC	[121]
MoP@NC-1//AC	70@ ~ 100	~ 20@2042	–	–	0.01–4	0.8 M KPF <sub>e</sub> /EC-DEC	[122]
N-MoSe <sub>2</sub> /G//AC	119@40	29@7212	3000	75.2 %	0.5–4	0.8 M KPF <sub>e</sub> /EC-DEC	[123]
Mo <sub>2</sub> C/NCNFs//AC	88@41	32@630	1000	80.4 %	0.01–3.8	1 M KFSI/EC-DEC	[124]
Sn//AC	120@240	57@2850	2000	~ 100 %	1–4	1 M KPF <sub>e</sub> /EC-DMC-EMC	[128]

Al, Ni, stainless steel as well as carbon-based and their composites)<sup>[155]</sup>, and other components that affect the overall performance of the device. Therefore, efforts must be made to explore the components that can adapt to positive and negative electrode materials to achieve high-performance PIHCs.

5) Currently, most characterization techniques focus on secondary batteries, such as lithium-ion batteries. At the same

time, some charge storage mechanisms of hybrid capacitors, especially the interface between electrodes and electrolytes and the redox mechanism, are still unclear and worthy of further exploration. Studies combining electrochemistry and various characterization techniques, such as *in situ* scanning electrochemical probe microscopy (SEPM), electrochemical quartz crystal microbalance (EQCM), sum-frequency generation spectroscopy (SFG), neutron reflectometer (NR), solid-

- state nuclear magnetic resonance (SS-NMR) and their combinations, may be required. Theoretical calculations and multiphysics simulations are also essential.
- 6) As we all know, SCs have good temperature performance but fast self-discharge behavior. However, the self-discharge phenomenon of the secondary battery is not apparent, but the ability to adapt to temperature is poor. Therefore, in addition to the performance evaluated in most of the papers, self-discharge behavior and temperature performance are the two criteria that are crucial to evaluate the actual performance and application value of PIHCs. We believe that high-performance PIHCs and related devices, which are capable of mass production, will be available in the near future.

## Acknowledgements

This work was supported by the National Natural Science Foundation of China (U1802256, 22209204, 22279162, 21975283), the Natural Science Foundation of Jiangsu Province (BK20221140), the China Postdoctoral Science Foundation (2022M713364), the Fundamental Research Funds for the Central Universities (2022QN1088), the Material Science and Engineering Discipline Guidance Fund of China University of Mining and Technology (CUMTMS202208).

## Conflict of Interests

The authors declare no conflict of interest.

## Data Availability Statement

The data that support the findings of this study are available from the corresponding author upon reasonable request.

**Keywords:** potassium-ion hybrid capacitors • electrode materials • energy storage mechanism • energy density • development prospect

- [1] Z. Zhu, T. Jiang, M. Ali, Y. Meng, Y. Jin, Y. Cui, W. Chen, *Chem. Rev.* **2022**, *122*, 16610.
- [2] Z. Wang, D. K. Denis, Z. Zhao, X. Sun, J. Zhang, L. Hou, C. Yuan, *J. Mater. Chem. A* **2019**, *7*, 18109.
- [3] L. Hou, R. Bao, Y. Zhang, X. Sun, J. Zhang, H. Dou, X. Zhang, C. Yuan, *J. Mater. Chem. A* **2018**, *6*, 17947.
- [4] J. Jiang, Y. Zhang, Y. An, L. Wu, Q. Zhu, H. Dou, X. Zhang, *Small Methods* **2019**, *3*, 1900081.
- [5] F. Zhang, J. Chen, G. Wallace, J. Yang, *Prog. Mater. Sci.* **2023**, 101069.
- [6] F. Zhang, J. Chen, J. Yang, *Adv. Fiber Mater.* **2022**, *4*, 720.
- [7] T. Kim, W. Song, D. Son, L. Ono, Y. Qi, *J. Mater. Chem. A* **2019**, *7*, 2942.
- [8] M. Su, J. Li, K. He, K. Fu, P. Nui, Y. Chen, Y. Zhou, A. Dou, X. Hou, Y. Liu, *J. Colloid Interface Sci.* **2023**, *629*, 83.
- [9] J. Xu, X. Cai, S. Cai, Y. Shao, C. Hu, S. Lu, S. Ding, *Energy Environ. Mater.* **2022**, *0*, e12450.
- [10] W. He, H. Xu, Z. Chen, J. Long, J. Zhang, J. Jiang, H. Dou, X. Zhang, *Nano-Micro Lett.* **2023**, *15*, 107.
- [11] X. Qu, H. Huang, T. Wan, L. Hu, Z. Yu, Y. Liu, A. Dou, Y. Zhou, M. Su, X. Peng, *Nano Energy* **2022**, *91*, 106665.
- [12] K. Kubota, M. Dahbi, T. Hosaka, S. Kumakura, S. Komaba, *Chem. Rec.* **2018**, *18*, 459.
- [13] P. Nie, M. Liu, W. Qu, M. Hou, L. Chang, Z. Wu, H. Wang, J. Jiang, *Adv. Funct. Mater.* **2023**, 2302235.
- [14] Q. Pan, Z. Tong, Y. Su, Y. Zheng, L. Shang, Y. Tang, *Adv. Mater.* **2022**, *34*, 2203485.
- [15] C. Han, H. Wang, Z. Wang, X. Ou, Y. Tang, *Adv. Mater.* **2023**, *35*, 2300917.
- [16] Q. Pan, Y. Zheng, Z. Tong, L. Shi, Y. Tang, *Angew. Chem. Int. Ed.* **2021**, *60*, 11835.
- [17] B. Li, J. Zheng, H. Zhang, L. Jin, D. Yang, H. Lv, C. Shen, A. Shellikeri, Y. Zheng, R. Gong, *Adv. Mater.* **2018**, *30*, 1705670.
- [18] Q. Xia, H. Yang, M. Wang, M. Yang, Q. Guo, L. Wan, H. Xia, Y. Yu, *Adv. Energy Mater.* **2017**, *7*, 1701336.
- [19] T. Hosaka, K. Kubota, A. S. Hameed, S. Komaba, *Chem. Rev.* **2020**, *120*, 6358.
- [20] M. Sajjad, F. Cheng, W. Lu, *RSC Adv.* **2021**, *11*, 25450.
- [21] M. Liu, L. Chang, Z. Le, J. Jiang, J. Li, H. Wang, C. Zhao, T. Xu, P. Nie, L. Wang, *ChemSusChem* **2020**, *13*, 5837.
- [22] J. Ding, W. Hu, E. Paek, D. Mitlin, *Chem. Rev.* **2018**, *118*, 6457.
- [23] P. Naskar, D. Kundu, A. Maiti, P. Chakraborty, B. Biswas, A. Banerjee, *ChemElectroChem* **2021**, *8*, 1393.
- [24] Y. Zhang, Z. Liu, X. Sun, Y. An, X. Zhang, K. Wang, C. Dong, Q. Huo, T. Wei, Y. Ma, *J. Energy Storage* **2019**, *25*, 100902.
- [25] Y. Xu, J. Ruan, Y. Pang, H. Sun, C. Liang, H. Li, J. Yang, S. Zheng, *Nano-Micro Lett.* **2021**, *13*, 1.
- [26] S. Chen, J. Wang, L. Fan, R. Ma, E. Zhang, Q. Liu, B. Lu, *Adv. Energy Mater.* **2018**, *8*, 1800140.
- [27] F. Li, Z. Zhou, *Small* **2018**, *14*, 1702961.
- [28] T. Li, H. Zhao, C. Li, W. Yu, Y. Shi, R. Wang, *New. Carbon. Mater.* **2021**, *36*, 253.
- [29] D. Gong, C. Wei, D. Xie, Y. Tang, *Chem. Eng. J.* **2022**, *431*, 133444.
- [30] C. Wei, D. Gong, D. Xie, Y. Tang, *ACS Energy Lett.* **2021**, *6*, 4336.
- [31] A. Le Comte, Y. Reynier, C. Vincens, C. Leys, P. Azaïs, *J. Power Sources* **2017**, *363*, 34.
- [32] K. Moyer, J. Donohue, N. Ramanna, A. P. Cohn, N. Muralidharan, J. Eaves, C. L. Pint, *Nanoscale* **2018**, *10*, 13335.
- [33] C. Meng, M. Yuan, B. Cao, Z. Jiang, J. Zhang, A. Li, X. Chen, M. Jia, H. Song, *J. Mater. Chem. A* **2022**, *10*, 22236.
- [34] H. Zhang, C. Wang, H. Luo, J. Chen, M. Kuang, J. Yang, *Angew. Chem. Int. Ed.* **2022**, *135*, e202217071.
- [35] S. Dong, Y. Song, Y. Fang, K. Zhu, K. Ye, Y. Gao, J. Yan, G. Wang, D. Cao, *Carbon* **2021**, *178*, 1.
- [36] Y. Sun, J. Zheng, F. Li, Y. Long, D. Xie, H. Li, M. Liu, *Appl. Mater. Today* **2023**, *30*, 101702.
- [37] Q. Li, T. Wang, T. Shu, Y. Miao, X. Pan, Y. Tao, J. Qi, Y. Sui, Y. He, Q. Meng, F. Wei, Y. Ren, Y. Zhao, Z. Ju, L. Wei, *J. Colloid Interface Sci.* **2022**, *621*, 169.
- [38] H. Liang, Y. Zhang, S. Hao, L. Cao, Y. Li, Q. Li, D. Chen, X. Wang, X. Guo, H. Li, *Energy Storage Mater.* **2021**, *40*, 250.
- [39] M. Hu, J. Song, H. Fan, L. Bai, Y. Wang, S. Liu, Y. Jin, Y. Cui, W. Liu, *Chem. Eng. J.* **2023**, *451*, 138452.
- [40] Y. Luan, R. Hu, Y. Fang, K. Zhu, K. Cheng, J. Yan, K. Ye, G. Wang, D. Cao, *Nano-Micro Lett.* **2019**, *11*, 30.
- [41] D. Qiu, J. Guan, M. Li, C. Kang, J. Wei, F. Wang, R. Yang, *Adv. Sci.* **2020**, *7*, 2001681.
- [42] D. Li, C. Liu, D. Huang, M. Zhang, X. Zhang, H. Gou, F. Yin, G. Wang, *Chem. Eng. J.* **2021**, *417*, 128048.
- [43] C. Wu, Q. Xu, H. Ning, Y. Zhao, S. Guo, X. Sun, Y. Wang, H. Hu, M. Wu, *Carbon* **2022**, *196*, 727.
- [44] Y. Wang, H. Wang, F. Sun, M. Zhang, R. Hou, Z. Yuan, *Rare Met.* **2022**, *41*, 3706.
- [45] C. Zhang, X. Liu, Z. Li, C. Zhang, Z. Chen, D. Pan, M. Wu, *Adv. Funct. Mater.* **2021**, *31*, 2101470.
- [46] W. Li, R. Zhang, Z. Chen, B. Fan, K. Xiao, H. Liu, P. Gao, J. Wu, C. Tu, J. Liu, *Small* **2021**, *17*, e2100397.
- [47] Y. Feng, S. Chen, J. Wang, B. Lu, *J. Energy Chem.* **2020**, *43*, 129.
- [48] Y. Liu, Q. Ru, Y. Gao, Q. An, F. Chen, Z. Shi, M. Zheng, Z. Pan, *Appl. Surf. Sci.* **2020**, *525*, 146563.
- [49] Y. Cui, W. Liu, X. Wang, J. Li, Y. Zhang, Y. Du, S. Liu, H. Wang, W. Feng, M. Chen, *ACS Nano* **2019**, *13*, 11582.
- [50] Y. Liu, Q. Liu, X. Liu, C. Zhao, R. Su, X. Luo, Z. Liu, A. Ying, *Small* **2022**, e2206895.

- [51] W. Feng, Y. Cui, W. Liu, H. Wang, Y. Zhang, Y. Du, S. Liu, H. Wang, X. Gao, T. Wang, *ACS Nano* **2020**, *14*, 4938.
- [52] S. Wei, X. Deng, M. Kundu, Z. Ma, J. Wang, X. Wang, *ChemElectroChem* **2022**, *9*, e202101715.
- [53] M. Chen, W. Liu, Y. Du, Y. Cui, W. Feng, J. Zhou, X. Gao, T. Wang, S. Liu, Y. Jin, *ACS Sustainable Chem. Eng.* **2021**, *9*, 3931.
- [54] Z. Xu, M. Wu, Z. Chen, C. Chen, J. Yang, T. Feng, E. Paek, D. Mitlin, *Adv. Sci.* **2019**, *6*, 1802272.
- [55] Z. Chen, W. Li, J. Yang, J. Liao, C. Chen, Y. Song, S. A. A. Shah, Z. Xu, M. Wu, *J. Electrochem. Soc.* **2020**, *167*, 050506.
- [56] Y. Qian, Y. Li, Z. Pan, J. Tian, N. Lin, Y. Qian, *Adv. Funct. Mater.* **2021**, *31*, 2103115.
- [57] T. Zhang, Z. Mao, X. Shi, J. Jin, B. He, R. Wang, Y. Gong, H. Wang, *Energy Environ. Sci.* **2022**, *15*, 158.
- [58] P. Wang, Z. Gong, K. Ye, Y. Gao, K. Zhu, J. Yan, G. Wang, D. Cao, *Appl. Surf. Sci.* **2021**, *553*, 149569.
- [59] X. Li, H. Wang, W. Zhang, W. Wei, R. Liao, J. Shi, M. Huang, S. Liu, Z. Shi, *Nanoscale* **2021**, *13*, 2389.
- [60] P. Cai, R. Momen, Y. Tian, L. Yang, K. Zou, A. Massoudi, W. Deng, H. Hou, G. Zou, X. Ji, *Adv. Energy Mater.* **2022**, *12*, 2103221.
- [61] J. Ruan, F. Mo, Z. Chen, M. Liu, S. Zheng, R. Wu, F. Fang, Y. Song, D. Sun, *Adv. Energy Mater.* **2020**, *10*, 1904045.
- [62] F. Yuan, J. Wang, H. Wang, D. Zhang, Z. Li, Q. Wang, H. Sun, Y. Wu, B. Wang, *Composites Part B* **2023**, *248*, 110379.
- [63] M. Shao, C. Li, T. Li, H. Zhao, W. Yu, R. Wang, J. Zhang, L. Yin, *Adv. Funct. Mater.* **2020**, *30*, 2006561.
- [64] H. Li, J. Chen, L. Zhang, K. Wang, X. Zhang, B. Yang, L. Liu, W. Liu, X. Yan, *J. Mater. Chem. A* **2020**, *8*, 16302.
- [65] H. Liang, Z. Sun, M. Zhang, W. Hu, J. Shi, J. Chen, W. Tian, M. Huang, J. Wu, H. Wang, *Energy Environ. Mater.* e12559.
- [66] D. Qiu, B. Zhang, T. Zhang, T. Shen, Z. Zhao, Y. Hou, *ACS Nano* **2022**, *16*, 12.
- [67] G. Zhu, R. Guo, W. Luo, H. Liu, W. Jiang, S. Dou, J. Yang, *Natl. Sci. Rev.* **2021**, *8*, nwaa152.
- [68] J. Cao, H. Xu, J. Zhong, X. Li, S. Li, Y. Wang, M. Zhang, H. Deng, Y. Wang, C. Cui, *ACS Appl. Mater. Interfaces* **2021**, *13*, 8497.
- [69] Y. Sun, J. Zheng, Y. Tong, Y. Wu, X. Liu, L. Niu, H. Li, *J. Colloid Interface Sci.* **2022**, *606*, 1940.
- [70] X. Liu, Y. Tong, Y. Wu, J. Zheng, Y. Sun, L. Niu, H. Li, *Chem. Eng. J.* **2022**, *431*, 133986.
- [71] D. Qiu, J. Guan, M. Li, C. Kang, J. Wei, Y. Li, Z. Xie, F. Wang, R. Yang, *Adv. Funct. Mater.* **2019**, *29*, 1903496.
- [72] D. Wang, Y. He, H. Liu, X. Xia, *Electrochim. Acta* **2022**, *428*, 140931.
- [73] M. Liu, L. Chang, J. Wang, J. Li, J. Jiang, G. Pang, H. Wang, P. Nie, C. Zhao, T. Xu, *J. Power Sources* **2020**, *469*, 228415.
- [74] B. Yang, J. Chen, L. Liu, P. Ma, B. Liu, J. Lang, Y. Tang, X. Yan, *Energy Storage Mater.* **2019**, *23*, 522.
- [75] F. Yuan, D. Zhang, Q. Yu, Z. Li, Q. Wang, H. Wang, Y. Wu, B. Wang, *Phys. Chem. Chem. Phys.* **2022**, *24*, 3440.
- [76] L. Yang, Z. Cao, J. Yin, C. Wang, D. Ouyang, H. Zhu, Y. Wang, L. Cavallo, H. N. Alshareef, J. Yin, *Small* **2023**, 2300440.
- [77] Z. Luo, Q. Zhang, W. Xie, T. Yuan, Q. Zang, N. Wang, H. Fan, S. Xie, X. Ouyang, *J. Alloys Compd.* **2022**, *914*, 165285.
- [78] G. Wang, W. Wang, X. He, J. Li, L. Yu, B. Peng, R. Liu, S. Zeng, G. Zhang, *Small* **2022**, *18*, 2203288.
- [79] Z. Xie, J. Xia, D. Qiu, J. Wei, M. Li, F. Wang, R. Yang, *Sustain. Energy Fuels* **2022**, *6*, 162.
- [80] G. Wang, W. Wang, X. He, J. Li, L. Yu, B. Peng, G. Zhang, *Energy Storage Mater.* **2022**, *46*, 10.
- [81] C. Zhang, Q. Li, T. Wang, Y. Miao, J. Qi, Y. Sui, Q. Meng, F. Wei, L. Zhu, W. Zhang, *Nanoscale* **2022**, *14*, 6339.
- [82] J. Gao, G. Wang, W. Wang, L. Yu, B. Peng, A. El-Harairy, J. Li, G. Zhang, *ACS Nano* **2022**, *16*, 6255.
- [83] L. Zhao, S. R. Sun, J. X. Lin, L. Zhong, L. H. Chen, J. Guo, J. Yin, H. N. Alshareef, X. Qiu, W. L. Zhang, *Nano-Micro Lett.* **2023**, 15.
- [84] J. Li, W. Qin, J. Xie, H. Lei, Y. Zhu, W. Huang, X. Xu, Z. Zhao, W. Mai, *Nano Energy* **2018**, *53*, 415.
- [85] Y. Zhang, W. Wei, C. Zhu, Z. Gao, J. Shi, M. Huang, S. Liu, H. Wang, *Electrochim. Acta* **2022**, *424*, 140596.
- [86] X. Hu, Y. Liu, J. Chen, L. Yi, H. Zhan, Z. Wen, *Adv. Energy Mater.* **2019**, *9*, 1901533.
- [87] B. Fan, J. Yan, A. Hu, Z. Liu, W. Li, Y. Li, Y. Xu, Y. Zhang, Q. Tang, X. Chen, *Carbon* **2020**, *164*, 1.
- [88] Y. Peng, R. Zhang, B. Fan, W. Li, Z. Chen, H. Liu, P. Gao, S. Ni, J. Liu, X. Chen, *Small* **2020**, *16*, 2003724.
- [89] S. Zhao, K. Yan, J. Liang, Q. Yuan, J. Zhang, B. Sun, P. Munroe, G. Wang, *Adv. Funct. Mater.* **2021**, *31*, 2102060.
- [90] H. Pham, J. Fernando, M. Horn, J. MacLeod, N. Motta, W. Doherty, A. Payne, A. Nanjundan, D. Golberg, D. Dubal, *Electrochim. Acta* **2021**, *389*, 138717.
- [91] Y. Qian, B. Wu, Y. Li, Z. Pan, S. Feng, N. Lin, Y. Qian, *Angew. Chem. Int. Ed.* **2023**, *62*, e202217514.
- [92] S. Dou, J. Xu, C. Yang, W.-D. Liu, I. Manke, W. Zhou, X. Peng, C. Sun, K. Zhao, Z. Yan, *Nano Energy* **2022**, *93*, 106903.
- [93] W. Wang, J. Zhou, Z. Wang, L. Zhao, P. Li, Y. Yang, C. Yang, H. Huang, S. Guo, *Adv. Energy Mater.* **2018**, *8*, 1701648.
- [94] H. Kim, J. Jo, J. Choi, N. Voronina, D. Ahn, T. Jeon, H. Yashiro, Y. Aniskevich, G. Ragoisha, E. Streltsov, *Energy Storage Mater.* **2021**, *40*, 197.
- [95] Y. Shen, X. Shen, M. Yang, J. Qian, Y. Cao, H. Yang, Y. Luo, X. Ai, *Adv. Funct. Mater.* **2021**, *31*, 2101181.
- [96] F. Ming, H. Liang, W. Zhang, J. Ming, Y. Lei, A.-H. Emwas, H. N. Alshareef, *Nano Energy* **2019**, *62*, 853.
- [97] S. Zhao, Z. Liu, G. Xie, X. Guo, Z. Guo, F. Song, G. Li, C. Chen, X. Xie, N. Zhang, B. Sun, S. Guo, G. Wang, *Angew. Chem. Int. Ed.* **2021**, *60*, 26246.
- [98] Y. Fang, R. Hu, K. Zhu, K. Ye, J. Yan, G. Wang, D. Cao, *Adv. Funct. Mater.* **2020**, *30*, 2005663.
- [99] M. Wu, W. Zheng, X. Hu, F. Zhan, Q. He, H. Wang, Q. Zhang, L. Chen, *Small* **2022**, *18*.
- [100] M. Naguib, M. Kurtoglu, V. Presser, J. Lu, J. Niu, M. Heon, L. Hultman, Y. Gogotsi, M. W. Barsoum, *Adv. Mater.* **2011**, *23*, 4248.
- [101] G. Zhu, H. Zhang, J. Lu, Y. Hou, P. Liu, S. Dong, Y. Zhang, X. Dong, *Mater. Today Sustain.* **2022**, 100226.
- [102] P. Lian, Y. Dong, Z. Wu, S. Zheng, X. Wang, S. Wang, C. Sun, J. Qin, X. Shi, X. Bao, *Nano Energy* **2017**, *40*, 1.
- [103] B. Cao, H. Liu, P. Zhang, N. Sun, B. Zheng, Y. Li, H. Du, B. Xu, *Adv. Funct. Mater.* **2021**, *31*.
- [104] Z. Zeng, W. Zhang, H. Ma, Y. Yi, X. Lian, X. Yang, R. Cai, W. Zhao, J. Sun, *Chem. Eng. J.* **2023**, 455.
- [105] C. Qian, R. Wang, K. Sun, W. Bao, *Int. J. Energy Res.* **2022**, *46*, 17976.
- [106] Z. Wang, P. Hong, H. Zhao, Y. Lei, *Adv. Mater. Technol.* **2023**, *8*, 2200515.
- [107] Y. Lou, P. Li, H. He, M. Zhang, *J. Alloys Compd.* **2023**, 937.
- [108] S. Ho, H. Tuan, *Chem. Eng. J.* **2023**, 452.
- [109] Z. Yen, B. Chang, S. Jhang, Y. Tuan, *ACS Appl. Energ. Mater.* **2023**, *6*, 2.
- [110] C. Zhao, T. Xu, B. Yu, *Adv. Mater.* **2023**, *35*, 2208096.
- [111] R. Bai, M. Zhang, X. Zhang, S. Zhao, W. Chen, N. Chen, P. Ji, M. Kurbanov, H. Wang, H. Gou, *ACS Appl. Mater. Interfaces* **2021**, *14*, 1478.
- [112] X. Li, D. Li, J. Cai, X. Zhang, C. Zhang, G. Wang, *J. Power Sources* **2022**, *533*, 231419.
- [113] S. Zhao, L. Dong, B. Sun, K. Yan, J. Zhang, S. Wan, F. He, P. Munroe, P. H. Notten, G. Wang, *Small* **2020**, *16*, 1906131.
- [114] S. Dong, Z. Li, Z. Xing, X. Wu, X. Ji, X. Zhang, *ACS Appl. Mater. Interfaces* **2018**, *10*, 15542.
- [115] J. Dai, C. Zhao, N. Yang, H. Wang, L. Liu, J. Yang, Q. Wang, W. Zhang, H. Hu, *J. Power Sources* **2022**, *518*, 230771.
- [116] Z. Zhang, M. Li, Y. Gao, Z. Wei, M. Zhang, C. Wang, Y. Zeng, B. Zou, G. Chen, F. Du, *Adv. Funct. Mater.* **2018**, *28*, 1802684.
- [117] G. Wang, Y. Li, Y. Liu, S. Jiao, B. Peng, J. Li, L. Yu, G. Zhang, *Chem. Eng. J.* **2021**, *417*, 127977.
- [118] M. Chen, L. Wang, X. Sheng, T. Wang, J. Zhou, S. Li, X. Shen, M. Zhang, Q. Zhang, X. Yu, J. Zhu, B. Lu, *Adv. Funct. Mater.* **2020**, *30*, 2004247.
- [119] Y. Luo, C. Wang, X. Wang, *J. Colloid Interface Sci.* **2021**, *600*, 820.
- [120] C. Chang, K. Chen, Y. Hsieh, C. Chang, H. Tuan, *ACS Nano* **2022**, *16*, 1486.
- [121] Y. Wang, Z. Zhang, G. Wang, X. Yang, Y. Sui, F. Du, B. Zou, *Nanoscale Horiz.* **2019**, *4*, 1394.
- [122] W. Zong, N. Chui, Z. Tian, Y. Li, C. Yang, D. Rao, W. Wang, J. Huang, J. Wang, F. Lai, *Adv. Sci.* **2021**, *8*, 2004142.
- [123] Y. Yi, Z. Sun, C. Li, Z. Tian, C. Lu, Y. Shao, J. Li, J. Sun, Z. Liu, *Adv. Funct. Mater.* **2020**, *30*, 1903878.
- [124] H. Min, X. Zhang, H. Shu, L. Luo, X. Zeng, Y. Liao, Z. Chen, X. Wang, *J. Alloys Compd.* **2021**, *888*, 161498.
- [125] Z. Wang, X. Yan, F. Wang, T. Xiong, M.-S. Balogun, H. Zhou, J. Deng, *Carbon* **2021**, *174*, 556.
- [126] L. Chen, Y. Zhang, C. Hao, X. Zheng, Q. Sun, Y. Wei, B. Li, L. Ci, J. Wei, *ChemElectroChem* **2022**, *9*, e202200059.
- [127] H. Ramasamy, B. Senthilkumar, P. Barpanda, Y. Lee, *Chem. Eng. J.* **2019**, *368*, 235.

- [128] J. Lang, J. Li, X. Ou, F. Zhang, K. Shin, Y. Tang, *ACS Appl. Mater. Interfaces* **2019**, *12*, 2424.
- [129] J. Ge, B. Wang, J. Wang, Q. Zhang, B. Lu, *Adv. Energy Mater.* **2020**, *10*, 1903277.
- [130] C. Lin, C. Yang, Y. Tuan, *Energy Storage Mater.* **2022**, *51*, 38.
- [131] H. Pham, N. Chodankar, S. Jadhav, K. Jayaramulu, A. Nanjundan, D. Dubal, *Energy Storage Mater.* **2021**, *34*, 475.
- [132] D. Wang, P. Wang, B. Lu, K. Ye, K. Zhu, Q. Wang, J. Yan, G. Wang, D. Cao, *ACS Appl. Energ. Mater.* **2021**, *4*, 13593.
- [133] Y. Cui, W. Feng, D. Wang, Y. Wang, W. Liu, H. Wang, Y. Jin, Y. Yan, H. Hu, M. Wu, *Adv. Energy Mater.* **2021**, *11*, 2101343.
- [134] G. Cheng, W. Zhang, W. Wang, H. Wang, Y. Wang, J. Shi, J. Chen, S. Liu, M. Huang, D. Mitlin, *Carbon Energy* **2022**, *4*, 986.
- [135] Z. Chen, A. Zhang, C. Geng, J. Xiong, P. Sun, N. Tu, Y. Chen, J. Jiang, Z. Ju, *Mater. Chem. Phys.* **2023**, *303*, 127835.
- [136] J. Gao, G. Wang, Y. Liu, J. Li, B. Peng, S. Jiao, S. Zeng, G. Zhang, *J. Mater. Chem. A* **2020**, *8*, 13946.
- [137] J. Liu, B. Kong, *Electrochim. Acta* **2021**, *378*, 138141.
- [138] C. Wang, P. Wang, D. Ouyang, N. Xue, X. Xue, Y. Zhang, H. Zhu, J. Yin, *Energy Fuels* **2022**, *36*, 12807.
- [139] L. Liu, Y. Lu, S. Wang, Y. Ding, Y. Chen, D. Qiu, D. Wang, J. Niu, J. Zhang, X. Chen, *J. Colloid Interface Sci.* **2022**, *620*, 24.
- [140] Y. Qin, Y. Xie, H. Zhao, C. Zhu, T. Li, S. Zhang, R. Wang, Y. Shi, L. Yin, *Chin. Chem. Lett.* **2022**, *33*, 1463.
- [141] R. Wang, S. Wang, D. Jin, Y. Zhang, Y. Cai, J. Ma, L. Zhang, *Energy Storage Mater.* **2017**, *9*, 195.
- [142] S. Geng, T. Zhou, M. Jia, X. Shen, P. Gao, S. Tian, P. Zhou, B. Liu, J. Zhou, S. Zhuo, *Energy Environ. Sci.* **2021**, *14*, 3184.
- [143] B. Yang, B. Liu, Y. Ding, J. Chen, *ACS Appl. Energ. Mater.* **2022**, *5*, 5766.
- [144] L. Liu, Y. Li, S. Wang, Y. Lu, J. Zhang, D. Wang, Y. Ding, D. Qiu, J. Niu, Y. Yu, *J. Colloid Interface Sci.* **2022**, *628*, 975.
- [145] L. Zhou, M. Zhang, Y. Wang, Y. Zhu, L. Fu, X. Liu, Y. Wu, W. Huang, *Electrochim. Acta* **2017**, *232*, 106.
- [146] R. Lobato-Peralta, J. Vazquez-Samperio, O. Perez, P. Acevedo-Pena, E. Reguera, K. Cuentas-Gallegos, *J. Energy Storage* **2020**, *31*.
- [147] M. Sha, L. Liu, H. P. Zhao, Y. Lei, *Energy Environ. Mater.* **2020**, *3*, 56.
- [148] Y. Xu, S. Duan, Y. Sun, D. Bin, X. Tao, D. Zhang, Y. Liu, A. Cao, L. Wan, *J. Mater. Chem. A* **2019**, *7*, 4334.
- [149] J. Xu, S. Dou, X. Cui, W. Liu, Z. Zhang, Y. Deng, W. Hu, Y. Chen, *Energy Storage Mater.* **2021**, *34*, 85.
- [150] L. Xue, Y. Li, H. Gao, W. Zhou, X. Lü, W. Kaveevivitchai, A. Manthiram, J. B. Goodenough, *J. Am. Chem. Soc.* **2017**, *139*, 2164.
- [151] K. Nayak, J. Grinblat, M. Levi, E. Levi, S. Kim, J. W. Choi, D. Aurbach, *Adv. Energy Mater.* **2016**, *6*.
- [152] V. Ramasamy, K. Kaliyappan, R. Thangavel, M. Seong, K. Kang, W. Chen, S. Lee, *J. Phys. Chem. Lett.* **2017**, *8*, 5021.
- [153] V. Ramasamy, B. Senthilkumar, P. Barpanda, S. Lee, *Chem. Eng. J.* **2019**, *368*, 235.
- [154] J. Ge, X. Yi, L. Fan, B. Lu, *J. Energy Chem.* **2021**, *57*, 28.
- [155] Q. Liu, M. Li, Y. Le, F. Zhao, M. Chang, L. Fang, Q. Hou, R. Wang, H. Xu, P. Nie, *Rare Met.* **2023**, *42*, 134.

---

 Manuscript received: May 30, 2023

Revised manuscript received: July 13, 2023

Accepted manuscript online: July 14, 2023

Version of record online: July 31, 2023